Spring 2008

Unsteady flow and heat transfer in periodic complex geometries for the transitional flow regime

Li-Kwen Chen

Department: Mechanical and Aerospace Engineering

UNSTEADY FLOW AND HEAT TRANSFER IN PERIODIC COMPLEX GEOMETRIES FOR THE TRANSITIONAL FLOW REGIME

by

LI-KWEN CHEN

A DISSERTATION

Presented to the Faculty of the Graduate School of the

MISSOURI UNIVERSITY OF SCIENCE AND TECHNOLOGY

In Partial Fulfillment of the Requirements for the Degree

DOCTOR OF PHILOSOPHY

in

MECHANICAL ENGINEERING

2008

Approved by:

K. O. Homan, Advisor
Darryl J. Alofs
Kakkattukuzhy M. Isaac
A. L. Crosbie
Barbara N. Hale

PUBLICATION DISSERTATION OPTION

This dissertation has been prepared in the form of three papers for publication. Pages 2–38, pages 39–67, and pages 68–94 have been prepared for the International Journal of Heat and Mass Transfer and are in the required style.

ABSTRACT

Diesel engines are facing significant challenges with upcoming changes in emissions standards. In general, meeting the increased emission standards will require a larger fraction of the engine heat rejection to occur in the vehicle cooling system. For certain applications, the surface geometry must also be such that it resists particulate fouling, precluding common interrupted surfaces such as louvered fins. Although acceptable continuous surface geometries such as bumped fin geometries are in use, the impacts of changing the parameters of this geometry are unknown. This study investigates the transport characteristics of bumped fins in the transitional flow regime using unsteady multi-dimensional solutions of the incompressible Navier-Stokes equations. In the first of three parts, a two-dimensional model is used to examine the impact of channel aspect ratio for fixed absolute bump height and corrugation angle. Oscillatory behavior is observed and critical Reynolds numbers determined for the onset of supercritical flow behavior. In the second part, two-dimensional simulations are performed which consider the variation in corrugation angle for a fixed aspect ratio and relative bump height. Corrugation angles ranging from 25 to 90° are examined and compared with the wavy channel limit and the singly grooved channel. The results reveal that even at a fixed aspect ratio, the shape of the bump cavity influences the stability of the flow and its transport behavior. In the third and final part, a detailed three-dimensional numerical investigation of a channel element with a width aspect ratio of 3.7 is presented. The critical Reynolds number and primary oscillation frequency is shown to be largely unchanged from the two-dimensional predictions. However, detailed characteristics of the oscillatory behavior are influenced by longitudinal vortices captured in the three-dimensional model. The predicted transport characteristics both increase but do so in such a way that the surface efficiency is nearly unchanged from that predicted by the two-dimensional model.

ACKNOWLEDGMENT

This dissertation would not have been accomplished if not for the help and encouragement of a number of people. I would like to thank Dr. Kelly Homan for being my advisor and guiding my research. Dr. Homan's knowledge and insight was very helpful throughout the entire process. I especially appreciate how he showed me ways to organize and lead a project. I would also like to thank the distinguished members of my committee, Dr. Darryl Alofs, Dr. Al Crosbie, Dr. Kakkattukuzhy Isaac and Dr. Barbara Hale. In addition, thanks to Adams Thermal Systems, Inc. for sponsoring my research project. Many thanks also to my former lab mates Steve Rucker, John Bridges, Kyle Benne, and Trent Taylor. We had a great time working together and sharing everything. A thank you also to all of the staff members of the Mechanical Engineering Department at Missouri S & T who have helped me over the past four years. Without their expertise and experience, my work would not have been accomplished so smoothly. Thanks to my all friends in Rolla, they make me feel warm in this lovely town even in the chilly weather. Thanks to my family in my hometown of Taiwan, they have continually encouraged me throughout this work. Finally, a huge thanks to my wife Yi-Fang for being incredibly understanding, supportive, and most of all, patient. She has taken wonderful care of our daughter, Johnna, and has always given one hundred percent support during this time.

TABLE OF CONTENTS

LIST OF ILLUSTRATIONS

PAPER 2

PAPER 3

LIST OF TABLES

1. INTRODUCTION

The development of surface geometries for the air side of compact heat exchangers is an area of longstanding technical importance. In many applications, interrupted surfaces such as offset strip fins or louvered fins provide the desired level of heat transfer enhancement at an acceptable level of pressure drop. However, for applications in which the air stream may contain a significant amount of particulate or chaff, continuous surfaces are strongly preferred as they reduce the tendency of the heat exchanger passages to clog. The present investigation is motivated by the desire to identify the range of geometric variables which provide favorable thermal-hydraulic performance for bumped fins. These bumped fins are a continuous surface geometry with a form midway between grooved and wavy channels. In the literature, this geometry is novel. Since the desired operating points are in the transitional Reynolds number range, the present investigation adopts a modeling approach based on the unsteady Navier-Stokes equations in order to model the transport dynamics.

The investigation is divided into three parts. In the first part, the impact of space ratio is considered for fixed absolute bump height and corrugatioin angle. In the second part, the impact of corrugation angle is treated for fixed aspect ratio and relative bump height. Finally, a three-dimensional model of a single geometry is analyzed and compared to the predictions of the two-dimensional models utilized in the first two parts of this investigation.

Impact of Periodicity Length on Convective Enhancement in Bumped Channel

Li-Kwen Chen and K. O. Homan
Department of Mechanical & Aerospace Engineering
Missouri University of Science & Technology
Rolla, Missouri 65409–0050, USA

Abstract

In this study, an incompressible two-dimensional transitional bumped channel flow simulation is performed to deal with convective heat transfer. The computational domain is spatially periodic, with a fully developed condition and isothermal boundary wall prevailing at a periodic length. The numerical schemes and procedures are described. The objective of the present work is to identify the impact of the channel space ratio on heat transfer enhancement. The underlying objective of this study is to identify the relevant fluid mechanisms present in channels that enhance heat transfer performance. Three aspect ratios (1.8, 3.0, and 3.9) at selective Reynolds numbers are compared to reveal the shear layer (Kelvin-Helmholtz vortex), Taylor-Görtler vortex, flow separation, and reattachment as air flows through periodically corrugated channels. The flow destabilization due to a self-sustained oscillatory flow induces heat transfer enhancement. The oscillatory behavior is identified by the perturbation velocity (u'), and perturbation amplitude parameter (χ) to distinguish the subcritical and supercritical regimes, thereby enabling determination of critical Reynolds numbers. The results of the computations are presented in terms of Nusselt number, Colburn j factor, friction factor, and goodness factor. Space- and time-averaged forms are also used to identify desirable space ratios for high heat transport efficiency and low power consumption. At supercritical conditions, increases in the space ratio increase the heat transfer and fricion

loss simultaneously although the increment in the friction loss is larger. The results show that the flow is more effectively destabilized for space ratios larger than 3.0.

Nomenclature

Dimensional quantities are denoted by a hat, *e.g.* $\hat{t}$.

Roman

f	local friction factor
H	channel height
j	local Colburn j factor
j/f	goodness factor
L	channel length
s	wall coordinate
$\mathbf{n}$	unit normal vector
Nu	Nusselt number
p	pressure
Pe	Peclet number
Pr	Prandtl number
Re	Reynolds number
T	temperature

t	time
u, v	velocity components

Greek

α	thermal diffusivity
β	corrugation angle
Γ	time period
χ	perturbation amplitude parameter
μ	dynamic viscosity
ν	kinematic viscosity
ρ	density
σ	perturbation amplitude growth rate
τ	wall shear stress
Ω	frequency
Ψ	arbitrary scalar
ψ	Dimensionless Streamline

Subscripts and Superscripts

b	bulk
c	center
cr	critical

H referenced to channel height

i inflow

∞ free stream

min maximum

min minimum

w wall

$-$ Time-and-Space-Averaged

1. INTRODUCTION

Diesel engine designers are facing significant challenges with upcoming changes in emissions standards. The radiator must not only meet greater heat rejection demands but must do so in a compact volume. For certain applications, the surface geometry must be such that it resists particulate fouling. Louvered fins are commonly used in automotive radiators to increase the surface area and initiate new boundary layer growth. The louvered fin surface is the standard geometry for an automotive radiator. However, the traditional interrupted fins such as louvered fins are not applicable for many agriculture and off-highway radiators due to core clogging concerns. In a typical Ag/off-highway radiator, the use of continuous fins reduces this clogging problem. Although acceptable serpentine air fin geometries such as a bumped fin are in use, the impacts of changing the parameters of this geometry are unknown. This study seeks to investigate the characteristics of bumped fins for use in Ag/off-highway radiators.

In order to enhance the heat transfer rate, engineers have developed enhanced extended heat transfer surfaces to replace traditional plain surfaces. The augmentation technique of enhancing extended surfaces is meant to improve surface geometries of radiators.

These geometries can generate irregularities due to secondary flows or boundary layer separations within fin channels, and lead to the destruction of boundary layers and regrowth [1]. Extended surfaces also increase pressure drops, thus increasing the power consumption and operation costs. Therefore, it is important for the optimum geometrical combinations to match both desirable increments of theheat transfer rate and pressure drop. Reducing the air-side resistance is an efficient method for improving the heat transfer and reducing thermal resistance because about 80% or more thermal resistance is caused by the air side of a heat exchanger. Two approaches can reduce the thermal resistance: Either by additional heat transfer area or by increasing the air-side heat transfer coefficient [2].

In general, for air-side applications, fin geometries are divided into two categories: interrupted and continuous surfaces. Louvered fins are the typical interrupted fins and effectively increase the convective heat transfer areas due to restarting of thermal boundary layers, which derive the average heat transfer coefficients of interrupted surfaces to be much higher than those of continuous surfaces. In addition, transverse vortices generated by interrupted surfaces are drastically benefit to ehnance the heat transport under a supercritical regime [3, 4]. Hatada and Senshu experimentally studied convex louver fins [5]. The streamflow visualization exibited that these fins broke the development of boundary layer flows to intensify the heat transfer. Both wavy fin and triangular fin are typical continuous fins [1, 2], which provide complete intermixing due to flow separations and reattachments within the channels [1]. Hwang $etal.$ presented detailed illustrations to explain the relevant fluid mechanisms of continuous surfaces pertaining to a 3-D wavy duct with the corrugation angles of 17.5° and 25° [6]. Two types of secondary flows generated by this periodic corrugated duct are called Kelvin-Helmholtz vortex and Taylor-Görtler vortex. Kelvin-Helmholtz vortices are so-called shear layers and Taylor-Görtler vortices are centrifugal instabilities caused by these concave regions. In addition, the corner kinks on the wall corners perpendicular to the streamwise can be observed.

From the numerical results of Guzman and Amon [7], a rough estimate of the periodic state for converging-diverging channel flows was studied with $Re = 130 - 750$, which revealed three successive bifurcation levels when Re was increasing, namely: one-frequency periodic flow, two-frequency quasiperiodic flow and three-frequency quasiperiodic flow before an aperiodic chaotic flow pattern. Once the flow pattern is chaotic, the supplementary random motions of fluid particles will intensify the heat transfer even more. O'Brien and Sparrow investigated a corrugated duct and obtained 2.5 times of heat transfer as comparied to a parallel-plate channel [8].

In early development of the flow destabilization theory, researchers used a single cavity to study fluid mechanisms as a fluid flows over it. These cavities may be divided into open and closed cavities according to their values of length-to-depth ratios [9, 10]. For open cavities (short notches), the boundary layer separates at the separation wall due to a sudden expansion and secondary vortices in the cavity deflect the external flow over the cavity.

Charwat $etal.$ focused attention on the open cavity regime [9]. From the experimental results of this study, the longitudinal heat transfer mechanisms in cavities are divided into three vertivcal aspects: heat conduction occurs between the wall and the cavity, viz an isothermal dead air sink; heat conduction to the free shear layer and mass convection of the fluid exchange between the cavity and the external flow. The weak separation vortex destabilizes the upstream corner and the strong recompression vortex produces a well-mixed region which displays the high heat transfer rate. In the middle portion of the cavity, three distinct layers improve heat transport, namely: the reverse flow layer, buffer layer, and shear layer which occupy the cavity floor, central region, and upper zone, respectively. Taken together, the vortices and layers produce bidirectional heat diffusion in the cavity.

Amon and Mikic found the large-scale mixing produced by spontaneous supercritical flow destabilization is responsible for the heat transfer enhancement as it is in turbulent flows. It is found that for the same power dissipation, the heat transfer in communicating channel

flow is up to 300% higher than that in flat channel flow due to the effects of counter-rotating vortices [11].

In the investigations of self-sustained oscillations, Ghaddar $etal.$ used rectangular grooved channels to disclose the way to distinguish the subcritical and supercritical flow regimes. Meanwile, various geometries possess various values of oscillatory frequencies [12]. Roberts provided a clever method to obtain the precise values of critical Reynolds numbers (Re_{cr}) by using a pertubation parameter [13]. A simplified two-dimensional wavy finned-tube exchanger was investigated by Comini et al. [14]. The results showed that Re_{cr} will decrease and then increase with increasing space ratio under the same corrugation angle. Both friction factor and Nusselt number increase with an increase of the corrugation angle but first increase and then decrease alnog increasing space ratio.

The objective of this paper is to present results from several different geometries of bumped channels by varying the space ratios and Reynolds numbers with the goal of identifying favorable geometric combination. In addition, various fluid mechanisms caused by periodically corrugated channel flow are studied, such as the boundary layer, shear layer, transverse vortex, flow separation, and reattachment. The intention of using different Reynolds numbers is to try to discover the critical Reynolds number for each pattern. Many references disclosed that a critical Reynolds number is an important value to judge if the flow has good characteristic of heat transfer and reduction of thermal resistance. The primary purpose of this research is to investigate the dominant characteristics of both velocity and temperature fields via various bumped channels with different geometries.

2. PROBLEM FORMULATION

2.1 Mathematical Model

The focus of the present investigation is a continuous channel with periodic bumps. Considering a periodic element which is suitably separated from the channel entrance and

exit, the flow may be presumed periodic. The transfer mechanisms then repeat periodically across the inlet and exit of a single module. The flow is then fully developed, both hydrodynamically and thermally, in a periodic sense. This approach has been adopted by numous previous investigators [4, 7, 12, 15]. In this paper,attention is focused on a periodic element of the channel with a dimensional length $\hat{L}$ and a dimensional height $\hat{H}_s$. The assumption of periodicity implies extensions in both and horizontal directions, as shown in Figure 1. The tensor forms of the dimensionless continuity, momentum, and energy equations can be written as

$$\frac{\partial u_i}{\partial x_i} = 0 \quad in\ D \tag{1}$$

$$\frac{\partial u_i}{\partial t} + \frac{\partial}{\partial x_j}(u_i u_j) = -\frac{\partial p}{\partial x_i} + \nu \frac{\partial^2 u_i}{\partial x_j \partial x_j} \quad in\ D \tag{2}$$

$$\frac{\partial T}{\partial t} + \frac{\partial}{\partial x_j}(T u_i) = \alpha \frac{\partial^2 T}{\partial x_j \partial x_j} \quad in\ D \tag{3}$$

Where the length scale is taken as $\hat{H}_s$, the velocity scale as $\hat{u}_\infty$, and the time scale as $\hat{H}_s/\hat{u}_\infty$. The definitions of the dimensions parameters are $Re_H \equiv \hat{u}_\infty \hat{H}_s/\nu$ and $Pe \equiv \hat{u}_\infty \hat{H}_s/\alpha$. Periodic boundary conditions are applied for velocity, pressure, and temperature according to the method originally proposed by Patankar et al. [16]. On the solid walls, the usual no-slip condition, $u = v = 0$, and a constant temperature boundary condition are used, $T = 0$. The inlet velocity is initially taken to be a uniform horizontal velocity, equal to that of the area-averaged dimensional velocity, $u = 1$, $v = 0$, and the initial inlet temperature as $T = 1$. The friction factor is defined in terms of the wall shear stress, τ_w, by

$$f = \frac{2\tau_w}{\rho u_\infty^2} \tag{4}$$

where $\tau_w = \mu \partial \mathbf{u}/\partial \mathbf{n}$ The heat transfer behavior is characterized by the Nusselt number, defined as

$$Nu = \frac{\frac{\partial T}{\partial n}|_w}{T_b} \tag{5}$$

where T_b is the dimensionless bulk mean temperature, defined as

$$T_b = \frac{\int_0^{H_s} |u(x,y,t)|T(x,y,t)dy}{\int_0^{H_s} |u(x,y,t)|dy} \tag{6}$$

The dimensionless heat transfer coefficient may be cast in the form of a Nusselt number or the Colburn j factor, related according to

$$j = \frac{Nu}{RePr^{1/3}} \tag{7}$$

Space and time-averaged values of the j and f are defined as

$$\Psi_s(t) = \frac{1}{S}\int_0^S \Psi(x,y,t)ds \tag{8}$$

$$\bar{\Psi} = \frac{1}{\Gamma}\int_t^{t+\Gamma} \Psi_s(t)dt \tag{9}$$

where s is the coordinate along the wall and Γ is a period of at least two oscillation cycles in length.

2.2 Numerical Method

The pre-processor GAMBIT 2.2.30 was used to generate grid points and cells. The solver FLUENT 6.2.16 was used to solve the fluid-dynamically and thermally algebraic equations cell by cell with various numerical schemes, and the post-processors C and TECPLOT 360 were used to evaluate and visualize the computed results. Referring to the algorithmic schemes of the solver, the finite-volume method and segregated scheme were used to solve these governing equations, with a second-order implicit scheme for time integration, a second-order scheme for solving pressure, and the third-order MUSCL (Monotone Upstream Scheme for Conservation Laws) scheme for solving the momentum and

temperature. The PISO (Pressure-Implicit with Splitting of Operator) scheme was used for solving pressure-velocity coupling.

Grid and time-step independence tests are crucial for the numerical study of any flow, particularly transitional flows, before initiating a sequence of simulation patterns. These preliminary calculations are established to verify the solutions are suitably independent of the various numbers of grid points and time step sizes. Hence, it is necessary to increase the grid points and decrease the time step sizes until a result is obtained which no longer changes with the different grid points and time step sizes [17].

The $L = 1.8$ geometry was chosen to proceed with the initial verification. By doubling the numbers of cells, the node numbers are 8,241 (8,000 cells), 16,281 (16,000 cells), and 32,481 (32,000 cells), respectively. Under the same $Re = 1,000$, time step sizes ($\triangle t$) of 0.002, 0.0002, and 0.00005 were selected. The values of $\bar{j_s}$ and $\bar{f_s}$ present a deviation smaller than 1% for cell numbers larger than 16,000 and $\triangle t$ smaller than 0.002. This result is regarded as grid and time-step independent. In this paper, the $L = 1.8$ geometry uses 16,000 cells (16,281 nodes) and the $\triangle t$ is 0.002, as shown in Figure 2 . Finer cell distributions are set near the boundary walls, the inlet and outlet, and the shear layer areas. The cell numbers were proportionally modified along with the different pattern sizes satisfy the CFL condition.

3. RESULTS AND DISCUSSION

The focus of the present investigation is the impact of channel aspect ratio, or space ratio, defined as $L = \hat{L}/\hat{H_s}$. Three geometries have been selected for consideration and are shown in Table 1. These geometries correspond to preserving a fixed dimensional element length, $\hat{L}$, and bump height, $\hat{H}$, while changing only the nominal channel width, $\hat{H}$.

3.1 Critical Reynolds Number

An important characteristic of laminar flows in periodic geometries is that once a critical Reynolds number has been exceeded, flow quantities display a regular oscillation with a constant frequency. At Reynolds numbers in the subcritical regime, integration from an arbitrary initial condition results in a time variation of dimensionless horizontal velocity perturbation, u', which asymptotes to zero. For supercitical Reynolds numbers, the oscillation amplitudes increase to a constant value. This difference enables straightforward identification of subcritical and supercritical flow conditions, as illustrated in Figure 3, for Reynolds numbers well above and below the critical Reynolds numbers. The perturbation velocity is defined as

$$u'(x, y, t) = u(x, y, t) - \frac{1}{\Gamma}\int_0^{\Gamma} u(x, y, t)dt \tag{10}$$

where Γ, the averaging period is at least two oscillation cycles. For the specific geometry shown in Figure 3, the critical Reynolds number, Re_{cr}, is clearly between 500 and 1,000.

Narrowing the range of the critical Reynolds number is made difficult with this approach, however, since the oscillation amplitudes become small as the critical Reynolds numbers approached from above. For this reason, Comini et al. [14] has indicated that the estimated value of the critical Reynolds number is likely to be larger than the true one. An alternative approach has been suggested by Roberts [13] in which the growth rate of a perturbation parameter based on the vertical velocity is used to determine quantitatively the critical Reynolds numbers. A change in the exponential growth rate of this quantity from negative to positive values then corresponds to the passage from subcritical to supercritical behavior for a given geometry. The Re_{cr} is recognized as the point for σ, which the growth

rate, is zero. The perturbation parameter, χ, is defined as

$$\chi = \frac{1}{S}\int_0^S |v(x, y_c, t)|ds \tag{11}$$

where y_c is the vertical center of the channel at every position x, and s is the coordinate measured along the path.

The variation of this perturbation parameter is shown in Figure 4 for the geometry $L = 1.8$. This perturbation parameter also indicates that the Re_{cr} lies between 500 and 1,000. Taking an exponential fit to these curves allows determination of an exponential growth constant, which allows quantitative determination of $Re_{cr} = 677$, as shown in Figure 5. By the same method, critical Reynolds numbers for the geometries $L = 3.0$ and 3.9 are determined to be 300 and 272, respectively. The Re_{cr} is central to determining how effectively a given channel geometry can enhance heat transfer.

3.2 Supercritical Oscillation Cycle

The importance of supercritical flow behavior to transport properties has been documented in numerous geometries such as grooved and wavy channels [10, 11, 13, 18, 19]. In the present study, the interest is in how supercritical flow behavior impacts transport properties for the bumped channel, specifically heat and momentum transfer.

Figure 6 shows the variation of f_s and j_s for the geometry $L = 1.8$ at sub- and supercritical Re. As expected, the space-averaged values, j_s and f_s, are steady in time under subcritical conditions. However, at a supercritical Re, the transport properties oscillate in time, as do components of the flow velocity.

The sequence of steps executed by the flow field during one of these oscillatory periods is shown in Figure 7. The bottom cavity contains both separation and recompression vortices for almost the entire cycle. However, at one point in the cycle the two vortices merge to produce a single vortex in the bottom cavity. Notably, this corresponds to the time in

the oscillatory period for which the heat transport is at its lowest value under supercritical conditions. In addition, this corresponds to the observed steady flow field under subcritical conditions, which displays a steady trapped vortex. Careful examination of Figure 7 also reveals that the vortices in the top cavities are varying in shape and intensity as time advances through the oscillatory cycle. The net result is an effective flow passage for the primary channel flow which is continuously varying, deflecting the main flow on a wavelength scaling with the periodicity length of the geometry.

At higher Reynold numbers, the flow transitions from a periodic to a quasi-periodic flow. For the geometry $L = 1.8$, multiple oscillatory frequencies are just perceptible in a plot of u' in time, as shown in Figure 8. Plots of the variation in time of j_s and f_s are shown in Figure 9. Interestingly, the secondary oscillation frequency is almost imperceptible in the plot of $j_s(t)$, but is much more evident in the plot of $f_s(t)$. Nevertheless, is quasi-periodic flow regime leads to an even more powerful and vigorous heat transfer enhancement than the periodic flow regime.

3.3 Space Ratio Effect

An effect immediately apparent upon variation of the space ratio is a change in the oscillation frequency. As shown in Table 2, the primary oscillation frequency decreases with an increase in the space ratio for subcritical Re condition. For a fixed space ratio, the oscillation frequency generally decreases with increasing Re. Interestingly, the change in the frequency of the least stable wave mode is lowest for the higher aspect ratio cases, since for $L = 1.8$, the frequency of the least-stable mode drops from 1.02 to 0.50 whereas for $L = 3.9$, the frequency drops from 0.41 to 0.35. As would be anticipated, a dramatic increase in heat transfer rate occurs when the flow passes into the supercritical flow regime. For example, with the geometry $L = 1.8$, the increase in time-and-space-averaged Nusselt number, $\overline{Nu}$, is over 80% when the flow becomes supercritical. The change in $\overline{Nu}$ for the subcritical Re is only a few percent.

As previously observed, the Re_{cr} decreased with increasing space ratio for the three geometries being considered. This leads to the expectation that heat transport will improve with increasing space ratio. The computed results indeed support this expectation as shown in Table 2. For a fixed Re, the $\overline{Nu}$ increases with the space ratio, L, for the supercritical flow regime. Also, for a fixed geometry, the increase in $\overline{Nu}$ is larger for the higher space ratio.

The time variation of the j_s and f_s are shown in Figure 10 for each of the space ratios investigated. The larger space-ratio patterns indeed display larger amplitude oscillations with evidence of quasi-periodic behavior. Interestingly, the j_s appears less sensitive to the flow oscillations than does the f_s.

The observation of significant oscillations in j_s and f_s leads naturally to the question of what flow structures correspond to the lows and highs in the transport behavior. The variation of j_s and f_s are shown in Figure 11 for the geometry $L = 3.0$, with the instants at which minimums and maximums occur denoted. The quasi-periodic behavior is evident, particularly in f_s. In addition, the oscillations in j_s and f_s are close to being out of phase.

The local variation of j and f at the instants of the minima and maxima in the space-averaged quantities are shown in Figure 12 and Figure 13. The variation in the j-factor is dominated by the temperature gradients at the lip of the cavity, $x \simeq 2.7$. The locally high values in the neighborhood of the bottom cavity opening, $x \simeq 0.3$, are comparable at the minima and maxima of j_s. These same observations hold true as well for the instants of minimum and maximum f_s, as shown in Figure 13.

The variation in f is also dominated by the flow dynamics in the neighborhood of the cavity exit bend, $x \simeq 2.7$. At the instant of maximum f_s, the f is concentrated near the bend but exhibits appreciable levels just prior to the entrance of the bottom cavity.

The dynamics of the previously described supercritical cycle are further clarified by consideration of the flow field at the instants of maxima and minima in the transport

properties. Instantaneous horizontal velocity profiles and streamlines at the instants of maximum and minimum j_s are shown in Figure 14 and Figure 15, respectively.

As denoted by Charwat et al. [9], the cavity walls may be referred to as a separation wall, a recovery wall, and a recompression wall. At instants of both maximum and minimum j_s, the flow separates at the start of the separation wall and reattaches at a point which oscillates in time, part way down the separation wall. The weak vortex between is called a separation vortex which varies in size and intensity. A second vortex, which may be termed a recompression vortex, exhibits large variation in size and intensity. At the instant of minimum j_s, its height is close to that of the cavity depth, $2H$, and is nearly centered in the cavity. However, at the instant of maxmimum j_s, this vortex has moved up along the recompression wall and is noticeably flattened. The impact on both the horizontal velocity and the temperature field along the recompression wall are noticeably high just prior to the cavity lip. The temperature contours shown in Figure 16, reveal much larger temperature gradients at the cavity exit at the instant of maximum j_s.

3.4 Literature Comparisons

Comparison of the present numerical values of $\bar{j}$ and $\bar{f}$ with published results for several channel geometries is shown in Figure 17. To investigate the improvement provided by different geometries, the wavy channel (L/H_s=2.2) of Comini et al. [14] exhibits the highest $\bar{j}$ and $\bar{f}$. It reveals the delimma in a modification of fin geometries to ehnance heat transport, viz resistance penalty and power consumption increase with complex channnels. Hatada and Senshu [5] and DeJong et al. [4] showed good heat transfer performance and moderate friction factors with the louvered fin and strip fin; however, these interrupted fins have clogging concerns. Comparisons of the present $\bar{j}$ values with those of the wavy channel, they all approach asymptotes of $\bar{j}$ when Reynolds numbers exceed specific values. That means the effect of Re increase has a limitation to enhace heat transfer for these geometries. These behaviors described above are decided by senondary vortices generated

with complex channels. The wavy channel can generate dominant secondary vortices at low Re, it manifests high values of $\bar{j}$ and $\bar{f}$ at the corresponding Re. On the other hand, the plain fin of Webb [1] hardly yields notable secondary vortices unless operated at high Re; it shows the lowest values of $\bar{j}$ and $\bar{f}$. Consequently, bumped channels are favorable choices given the moderate $\bar{j}$, low $\bar{f}$ and avoid the clogging concerns.

4. CONCLUSIONS

This paper has numerically investigated the hydrodynamic and thermal behavior of bumped channels with three different space ratios $L = 1.8$, 3.0, and 3.9. The flow exhibits high heat transport and relatively low friction loss once the Reynolds number exceeds a critical Reynolds number. Results presented here have shown that, compared to different space ratios, the larger space ratio patterns have smaller Re_{cr} and larger values of j_s, f_s at the same Re. The longer periodic lengths allow for more thorough mixing within the channels leading to enhancement in the heat transfer performance. The results also reveal that with increasing space ratios, friction factors increase but heat transfer effects are not significantly enhanced as long as the flow is under the subcritical regime. Referring to the comparison of transport properties, the subcritical Re is not anticipated as a desirable operating condition.

A relatively precise Re_{cr} can be obtained by the calculation of the growth rates in an amplitude factor based on the vertical velocity profile along the channel centerline. In addition, when the Re value increases from 1,000 to 2,000 ($L = 1.8$), the flow transitions from a periodic flow to a quasiperiodic flow, the value of Ω also develops from a single value primary frequency to two frequencies superimposed. This quasiperiodic flow regime provides even greater heat transfer enhancement than the periodic flow regime.

References

[1] R. L. Webb, Principles of enhanced heat transfer, John Wiley & Sons (1994).

[2] R. Webb, P. Trauger, Flow structure in the louvered fin heat exchanger geometry, *Experimental Thermal and Fluid Science* 4 (1991): 205–217.

[3] N. C. DeJong, A. M. Jacobi, Localized flow and heat transfer in louvered-fin arrays, *International Journal of Heat and Mass Transfer* 46 (2003): 443–455.

[4] N. C. DeJong, L. Zhang, A. M. Jacobi, S. Balachandar, D. Tafti, A complementary experimental and numerical study of the flow and heat transfer in offset strip-fin heat exchangers, *Journal of Heat Transfer* 120 (1998): 690–698.

[5] T. Hatada, T. Senshu, Experimental study on heat transfer characteristics of convex louver fins for air conditioning heat exchangers, Technical Report 84-HT-74, ASME paper (1984).

[6] S. D. Hwang, H. H. Kim, H. H. Cho, Heat transfer in wavy duct with different corrugation angle, in: ASME International Mechanical Engineering Congress (2002).

[7] G. A. M., C. H. Amon, Transition to chaos in convergingÂ-diverging channel flows: Ruelle- takens-newhouse scenario, *Physics of Fluids* 6 (1994): 1994–2002.

[8] J. E. O'Brien, E. M. Sparrow, Corrugated-duct heat transfer, pressure drop and flow visualization, *ASME J. Heat Transfer* 104 (1982): 410–416.

[9] A. F. Charwat, J. N. Roos, F. C. Dewey, Jr., J. A. Hitz, An investigation of separated flows-part i. the pressure field, *Journal of the Aerospace Sciences* 28 (1961): 457–470.

[10] A. F. Charwat, F. C. Dewey, Jr., J. N. Roos, J. A. Hitz, An investigation of separated flows-part ii: Flow in the cavity and heat trasfer, *Journal of the Aerospace Sciences* 28 (1961): 513–527.

[11] C. H. Amon, A. T. Patera, Numerical calculation of stable three-dimensional tertiary states in grooved-channel flow, *Physics of Fluids A* 1 (1989): 2005–2011.

[12] N. K. Ghaddar, K. Z. Korczak, B. B. Mikic, A. T. Patera, Numerical investigation of incompressible flow in grooved channels. part 1. stability and self-sustained oscillations, *Journal of Fluid Mechanics* 163 (1986): 99–127.

[13] E. P. L. Roberts, A numerical and experimental study of transition processed in an obstructed channel flow, *Journal of Fluid Mechanics* 260 (1993): 185–209.

[14] G. Comini, C. Nonino, S. Savino, Effect of space ratio and corrugation angle on convection enhancement in wavy channels, *Int J Num Methods Heat & Fluid Flow* 13 (2003): 500–519.

[15] M. Greiner, R. J. Faulkner, V. T. Van, H. M. Tufo, P. F. Fischer, Simulations of three-dimensional flow and augmented heat transfer in a symmetrically grooved channel, *ASME J. Heat Transfer* 122 (2000): 653–660.

[16] S. Patankar, C. Liu, E. Sparrow, Fully developed flow and heat transfer in ducts having streamwise-periodic variation of cross-sectional area, *Journal of Heat Transfer* 39 (1977): 80–86.

[17] J. D. Anderson, Computational Fluid Dynamics: The Basics with Applications, McGraw-Hill College (1995).

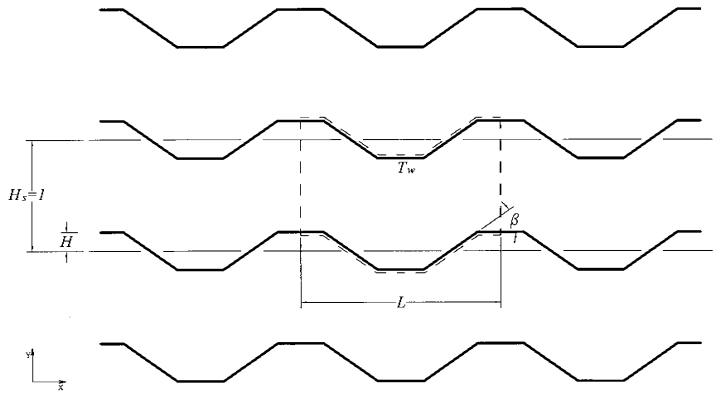

Figure 1 Schematic of a bumped channel passage with the dashed line indicating the periodic computational domain.

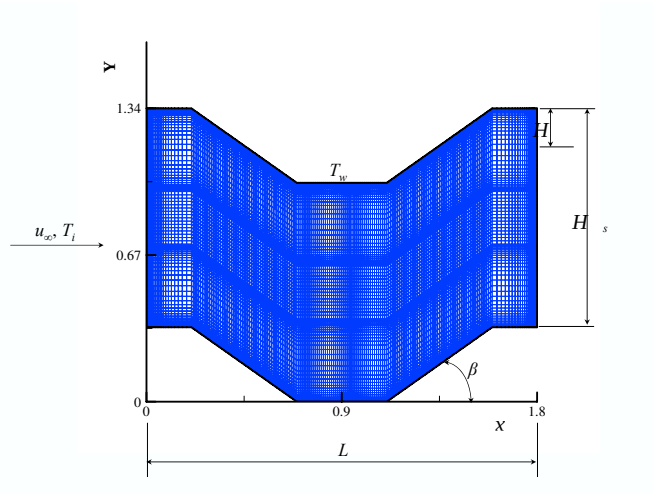

Figure 2 Grid layout for the geometry $L = 1.8$. The grid shown has 16,000 Cells (16,281 nodes) with a minimum $\triangle x = 0.0036$. The time step used with this grid was $\triangle t = 0.002$ for a CFL number of 0.55.

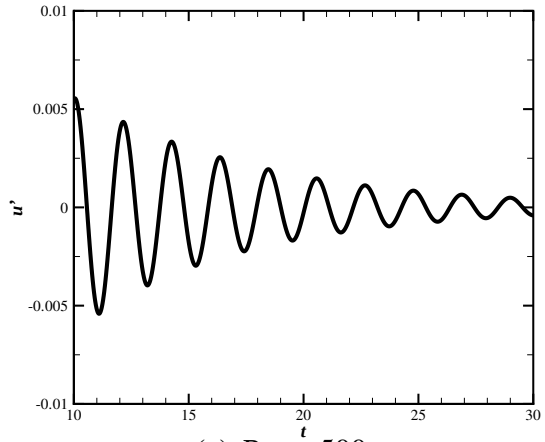

(a) $Re = 500$

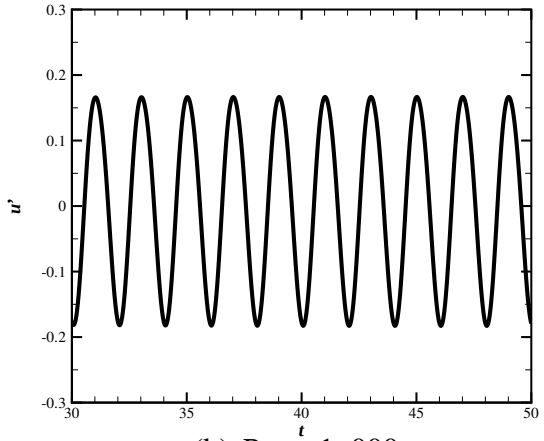

(b) $Re = 1,000$

Figure 3 Perturbation velocity versus time, $u'(t)$, at the position $x = 0.9$, $y = 0.36$ for geometry $L = 1.8$.

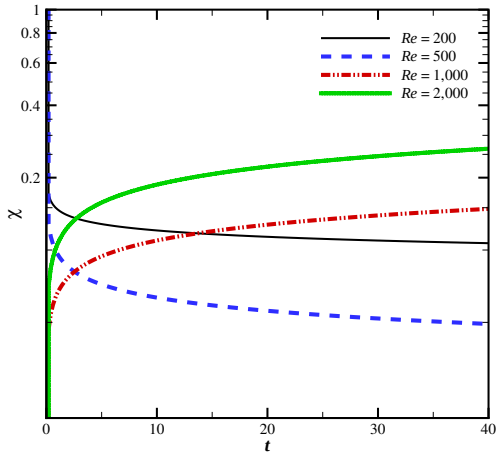

Figure 4 Time variation of perturbation parameter, $\chi(t)$, in time for the geometry $L = 1.8$ at selected Reynolds numbers.

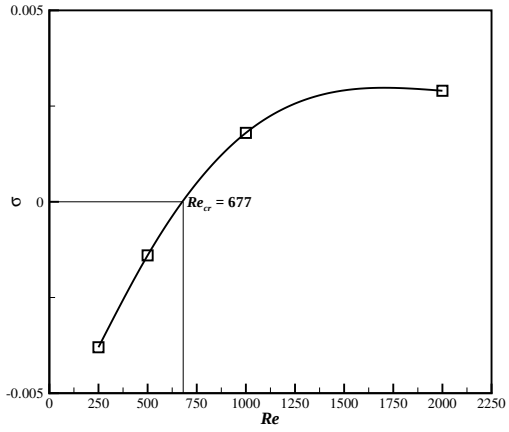

Figure 5 Instability growth rate versus Reynolds number for the geometry $L = 1.8$.

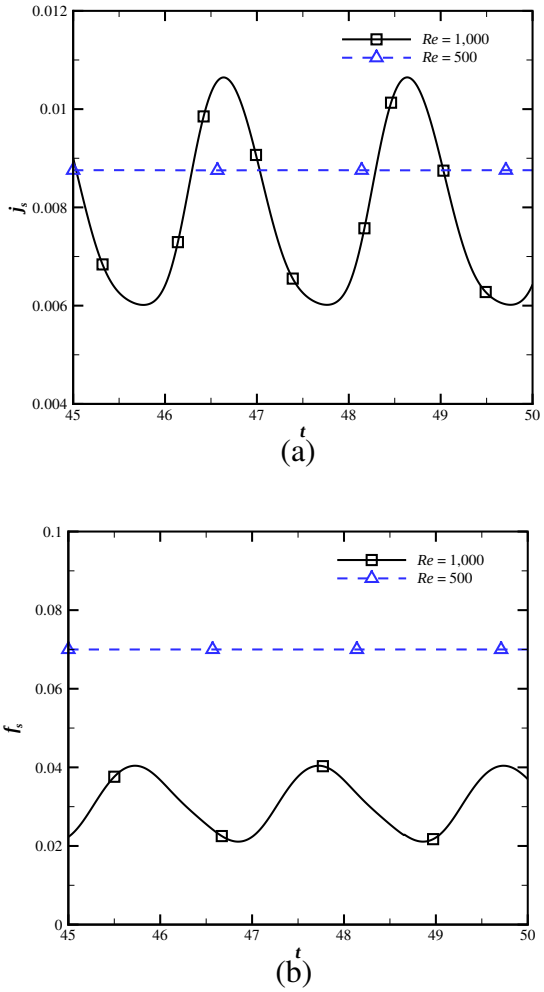

Figure 6 Comparison of time variation for space-averaged transport quantities for the geometry $L = 1.8$ at subcritical and supercritical Reynolds numbers.

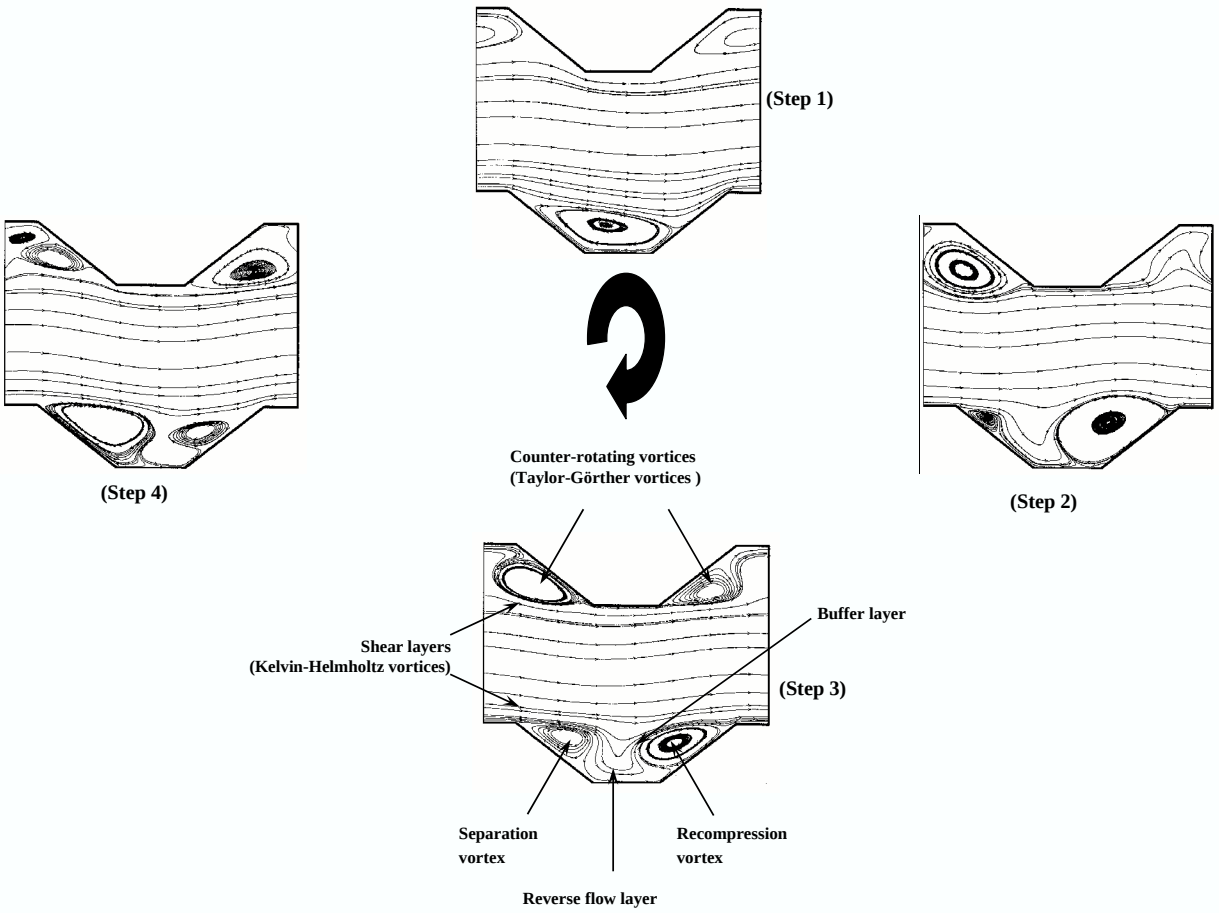

Figure 7 Instantaneous streamlines showing key stages in the cycle for periodic flow for the geometry $L = 1.8$ at $Re = 1,000$.

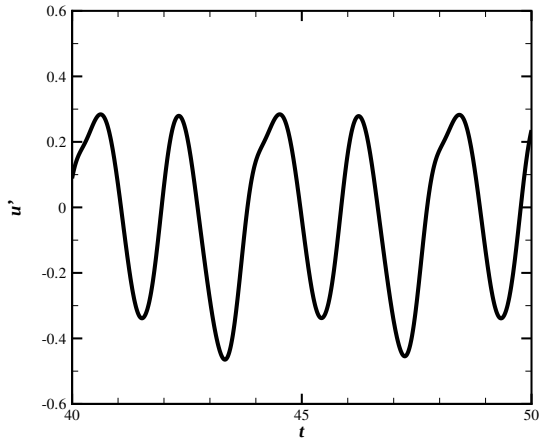

Figure 8 Time variation of perturbation velocity in quasiperiodic flow regime for the geometry $L = 1.8$ at $Re = 2,000$. The primary oscillation frequency is $\Omega \simeq 0.45$.

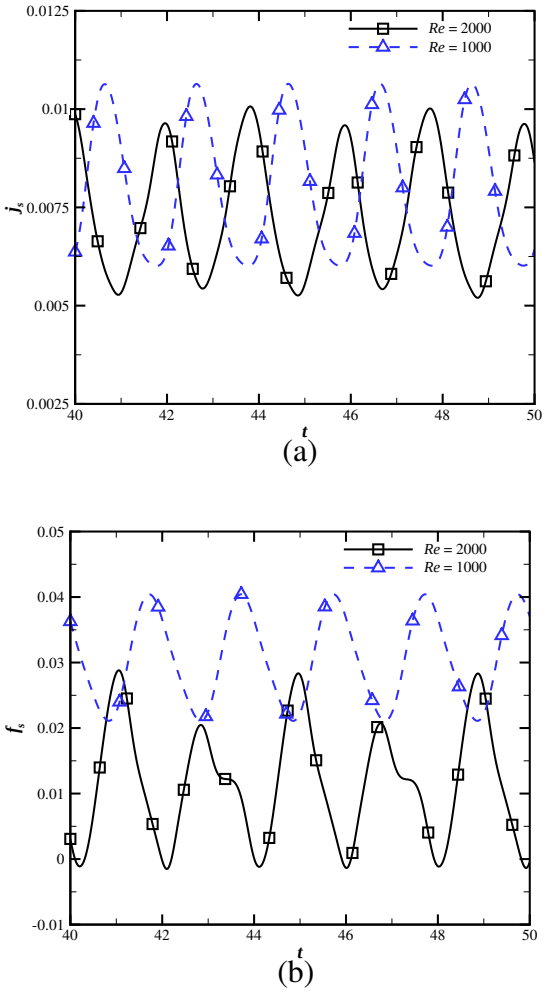

Figure 9 Time variation of transport quantities in the periodic and quasiperiodic flow regimes for the geometry $L = 1.8$.

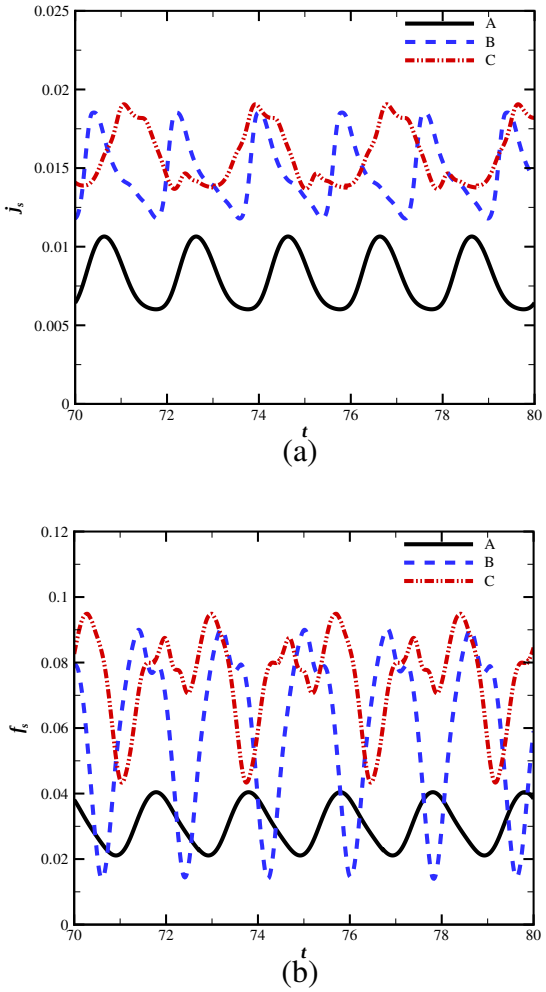

Figure 10 Impact of the space ratio on the time variation of space-averaged transport quantities for each geometry at $Re = 1,000$.

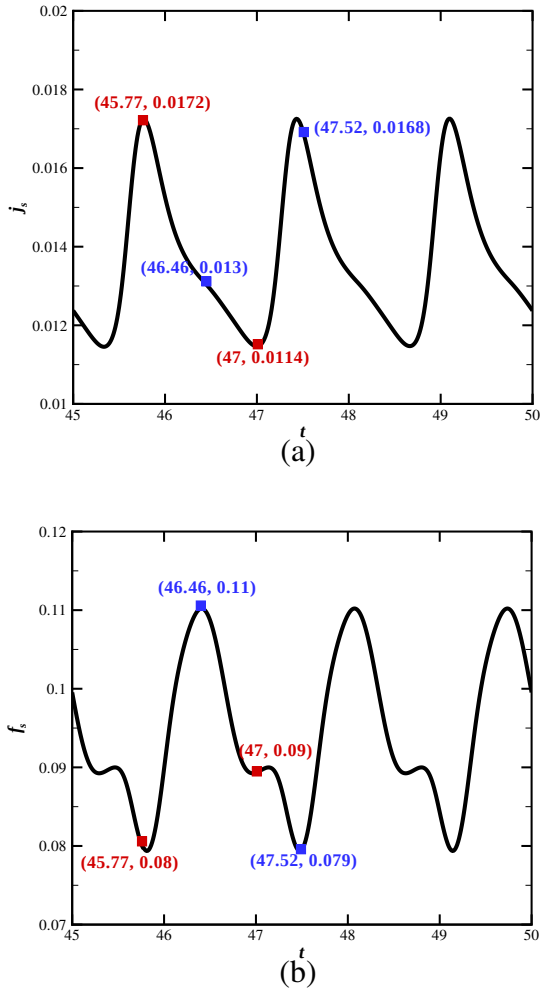

Figure 11 Time variation of space-averaged j and f factors for the geometry $L = 3.0$ at $Re = 500$.

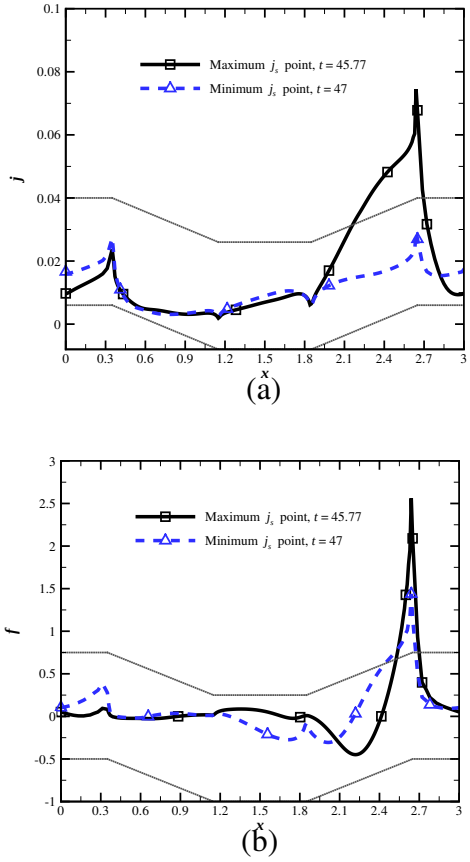

Figure 12 Streamwise variation of j- and f-factors along the bottom wall of the geometry $L = 3.0$ at $Re = 500$ for the instant of minimum and maximum j_s.

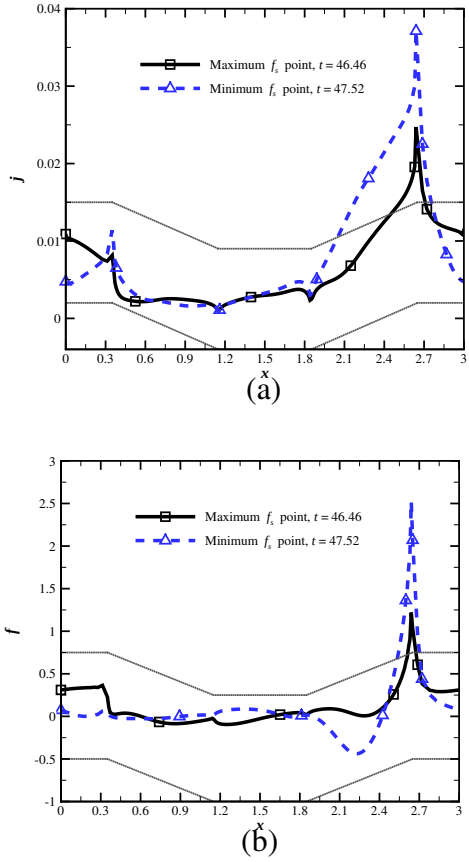

Figure 13 Streamwise variation of j- and f-factors along the bottom wall of the geometry $L = 3.0$ at $Re = 500$ for the instant of minimum and maximum f_s.

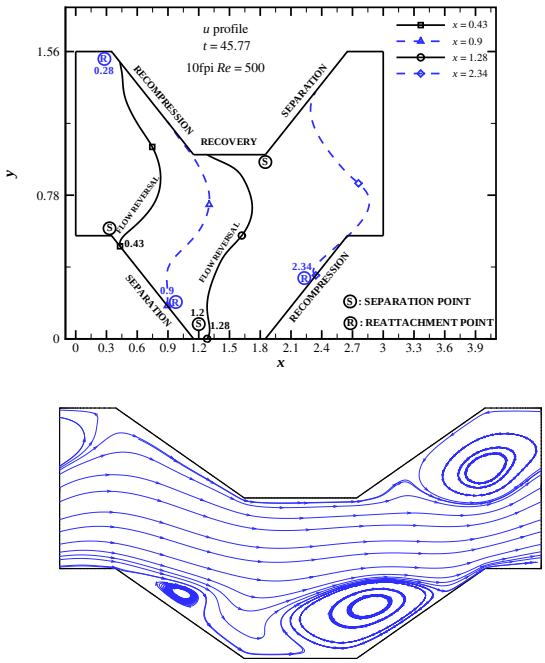

Figure 14 Instantaneous horizontal velocity profiles, $u(t, x)$, and streamlines, $\psi(t, x)$ at the instant of maximum j_s for the geometry $L = 3.0$ at $Re = 500$.

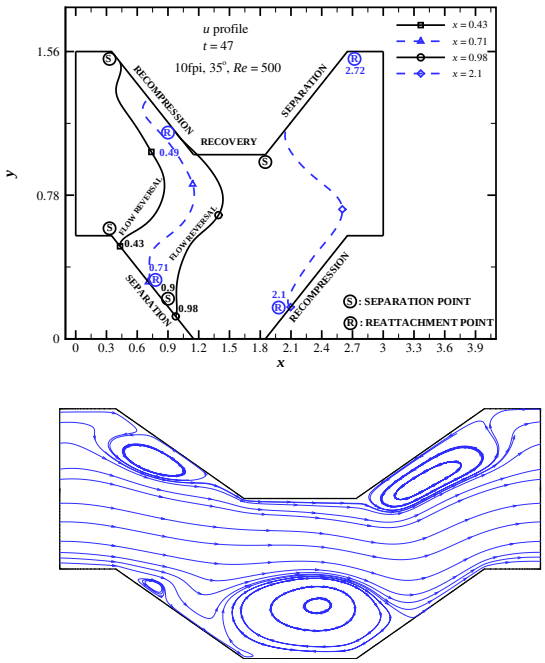

Figure 15 Instantaneous horizontal velocity profiles, $u(t, x)$, and streamlines, $\psi(t, x)$ at the instant of minimum j_s for the geometry $L = 3.0$ at $Re = 500$.

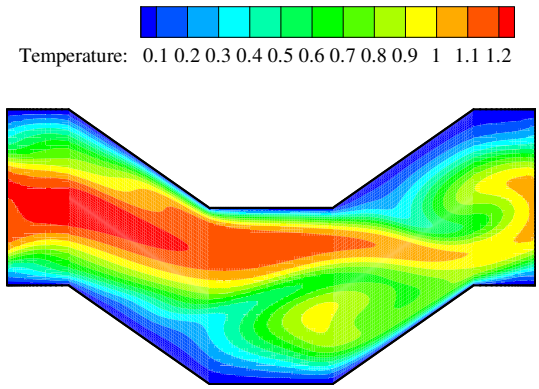

(a)

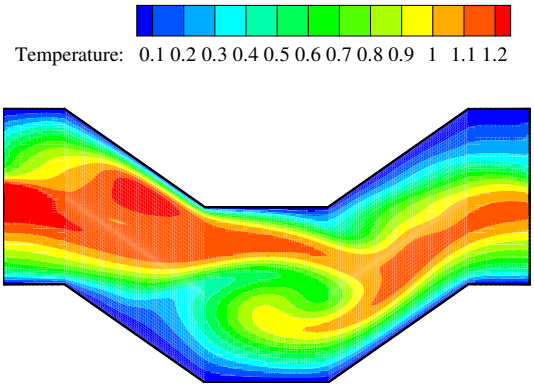

(b)

Figure 16 Temperature contours at instants of maximum ($t = 45.77$) and minimum ($t = 47.00$) space-averaged j-factor, j_s, for the geometry $L = 3.0$ at $Re = 500$.

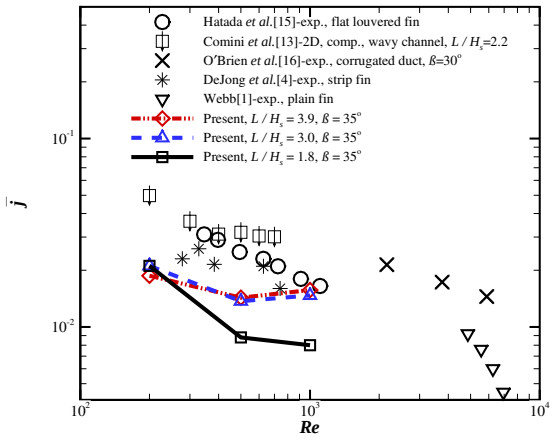

(a) $\bar{j}$ versus Re

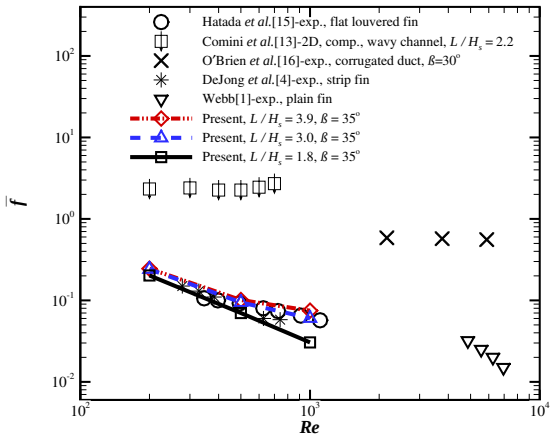

(b) $\bar{f}$ versus Re

Figure 17 Present results of $\bar{j}$ and $\bar{f}$ compared with other literatures' results.

Table 1 Geometric parameters for each of the bumped channel patterns considered, $\beta = 35°$.

Pattern	A	B	C
$L = \hat{L}/\hat{H}_s$	1.8	3	3.9
$H = \hat{H}/\hat{H}_s$	0.17	0.28	0.36

Table 2 Impact of space ratio, L, on time-and-space-averaged transport quantities.

Pattern	L	Re	Ω	$\overline{Nu}$	$\bar{j}$	$\bar{f}$	$\bar{j}/\bar{f}$
A	1.8	200*	1.02	3.74	0.0211	0.2022	0.104
		500*	0.48	3.98	0.0088	0.0700	0.126
		1,000**	0.50	7.10	0.0080	0.0305	0.262
B	3.0	200*	0.59	3.75	0.0211	0.2410	0.088
		500**	0.60	6.08	0.0137	0.0945	0.145
		1,000**	0.56	13.01	0.0147	0.0603	0.243
C	3.9	200*	0.41	3.32	0.0187	0.2450	0.076
		500**	0.35	6.34	0.0143	0.1010	0.141
		1,000**	0.35	13.97	0.0157	0.0748	0.210

* Subcritical
** Supercritical

Impact of Corrugation Angle on Convective Enhancement in Bumped Channel

Li-Kwen Chen and K. O. Homan
Department of Mechanical & Aerospace Engineering
Missouri University of Science & Technology
Rolla, Missouri 65409–0050, USA

Abstract

The previous study compared the thermal and hydrodynamic performance of bumped channels with three different space ratios. The objective of this paper is to numerically present the results from several different geometries by varying only the corrugation angle. Relative bump height and space ratio are held fixed. Seven different corrugation angles are studied parametrically, ranging from 25 to 90 degrees, and compared with the wavy channel and grooved channel limits under the same space ratio and relative bump height at a supercritical Reynolds number, $Re = 500$. Attention is focused on the influence of corrugation angles on the heat transfer and friction loss of bumped channels. In addition, fluid mechanism transitions caused by different corrugation angles are studied via overall and local performance for investigating the critical characteristics to enhance heat transfer. The wavy channel proves to be the highest efficiency, albeit with the lowest heat transfer. For corrugation angles between 30 and 65°, the surface efficiency is essentially constant as the j-factor increases monotonically. The grooved geometry has a markedly lower surface efficiency and lower amplitude oscillations, indicating a relatively higher critical Reynolds number.

Nomenclature

Dimensional quantities are denoted by a hat, *e.g.* $\hat{t}$.

Roman

f	local friction factor
H	channel height
j	local Colburn j factor
j/f	goodness factor
L	channel length
s	wall coordinate
$\mathbf{n}$	unit normal vector
Nu	Nusselt number
p	pressure
Pe	Peclet number
Pr	Prandtl number
Re	Reynolds number
T	temperature
t	time
u, v	velocity components

Greek

α	thermal diffusivity
β	corrugation angle

Γ	time period
χ	perturbation amplitude parameter
μ	dynamic viscosity
ν	kinematic viscosity
ρ	density
σ	perturbation amplitude growth rate
τ	wall shear stress
Ω	frequency
Ψ	arbitrary scalar
ψ	Dimensionless Streamline

Subscripts and Superscripts

b	bulk
c	center
cr	critical
H	referenced to channel height
i	inflow
∞	free stream
min	maximum
min	minimum

w wall

$-$ Time-and-Space-Averaged

1. INTRODUCTION

The idea of changing corrugation angles to enhance heat transport is common way in heat exchanger modification. Such transformations are based on the original space ratios and geometries, which is efficient for research and development. A number of published experimental and numerical results regarding changing corrugation angles such as louver and wavy fins. However, only a few attempts have been made to study the influence between a wide range of angle changes and fin performance.

An increase in the corrugation angle with constant space ratios will strengthen both heat transfer and thermal resistance. This intensity of heat transport is generally accompanied by much more increase in pressure drop, which causes the goodness factor to decrease. Some evaluation criteria will be guides for selecting the most favorable angle. Zhang and Lang performed experimental analysis of louvered fins with six different angles [1]. A trade-off method was utilized to indicate that $\beta = 20^\circ$ is suitable for automobile radiators and $\beta = 25^\circ$ is selected for locomotive radiator design. Suga and Aoki experimentally and numerically investigated multilouvered fins with various space ratios and corrugation angles under different Reynolds numbers [2]. Their study illustrated an easy way to utilize the contour maps of air temperature distributions and flow patterns to state the relationships of heat transfer between airflow and the number of louvers. In the range of $20^\circ \leq \beta \leq 30^\circ$, the optimum fin geometry with a smaller louver angle performed well in terms of both heat transfer and pressure drop.

Hatada and Senshu experimentally studied on heat transfer characteristics of convex louver fins for air conditioning heat exchangers [3]. For $\beta = 20^\circ$, the j factor and the f factor of convex louver fins are 14% and 8% higher than those of flat louver fins. Meanwhile,

the f factor severely increased $\beta = 24.6°$. A specific heat quantity and a specific fan power were introduced for evaluating heat exchanger fins in this study.

DeJong and Jacobi presented an investigation of flow, heat transfer, and pressure drop of louvered fins with Reynolds numbers from 130 to 1,400 [4]. The results indicated that the low transfer coefficients were related to low velocities between the louvers caused by thick velocity boundary layers. To minimize the heat transfer penalty, the size of the louver gap may increase by increasing the louver angle of the first row or two downstream to minimize the recovery zone. Decreasing the length of the recovery zone is beneficial to heat transport. For a small louver angle of 18°, the average heat trasport decreases to a maximum of 7% at a Reynolds number of 130 due to the long recovery zone.

Comini et al. [5] adopted a two-dimensional simulation to examine laminar air flows through wavy finned-tube exchangers by neglecting the influence of tubes. Numerical solutions were presented for space ratios H/L ranging from 0.1 to 0.45, and two corrugation angles of 20° and 30°. The solutions indicated that the critical Reynolds number differs with different geometric combinations. Both the friction factor and Nusselt number increase along the corrugation angle increases. Nevertheless, the friction factor and Nusselt number increase but only up to a certain space ratio when the space ratio increases. This discovery showed that the optimum value of the space ratio depends on both the corrugation angle and the Reynolds number.

This paper presents numerical results comparing bumped channels in different corrugation angles with wavy and grooved channels under $Re = 500$ to avoid subcritical or unsteady flow. The objective is to analyze the newly developed complex heat exchangers.

2. PROBLEM FORMULATION

2.1 Mathematical Model

When a numerical domain is assumed to be both hydrodynamically and thermally fully developed, suitably separated from channel the inflow and outflow effects, computational domain can be limited to a single module. After a certain distance from the channel inlet, transfer mechanisms will repeat periodically from the inlet to the outlet. In the fully developed region, this repetition allows for analysis of a single module with one periodic length only [6]. Mesh distributions and time step sizes ($\triangle t = 0.002$) of each computational module are based on the previous study. Cell numbers were proportionally modified along with the different pattern sizes shown in Table 1 (referring to the baseline geometry as $\beta = 35°$ shown in Figure 1).

The tensor forms of the dimensionless continuity, momentum, and energy equations can be written as

$$\frac{\partial u_i}{\partial x_i} = 0 \quad in\ D \tag{1}$$

$$\frac{\partial u_i}{\partial t} + \frac{\partial}{\partial x_j}(u_i u_j) = -\frac{\partial p}{\partial x_i} + \nu \frac{\partial^2 u_i}{\partial x_j \partial x_j} \quad in\ D \tag{2}$$

$$\frac{\partial T}{\partial t} + \frac{\partial}{\partial x_j}(T u_i) = \alpha \frac{\partial^2 T}{\partial x_j \partial x_j} \quad in\ D \tag{3}$$

Where the length scale is taken as $\hat{H}_s$, the velocity scale as $\hat{u}_\infty$, and the time scale as $\hat{H}_s/\hat{u}_\infty$. The definitions of the dimensions parameters are $Re_H \equiv \hat{u}_\infty \hat{H}_s/\nu$ and $Pe \equiv \hat{u}_\infty \hat{H}_s/\alpha$. Periodic boundary conditions can applied for velocity, pressure, and temperature according to the method originally proposed by Patankar et al. [7].

On the solid walls, the usual no-slip and a constant temperature boundary condition are used, $u = v = 0$ and $T = 0$. In the entrance region, the inlet velocity is initially taken to be a uniform horizontal velocity, equal to that of the area-averaged dimensional velocity, $u = 1$, $v = 0$, and $T = 1$. In the fully developed region, the friction factor can be

represented in terms of the wall shear stress, τ_w, by:

$$f = \frac{2\tau_w}{\rho u_\infty^2} \tag{4}$$

The heat transfer behavior is characterized by the Nusselt number, defined as

$$Nu = \frac{\frac{\partial T}{\partial n}|_w}{T_b} \tag{5}$$

where T_b is the dimensionless bulk mean temperature, which can be defined as

$$T_b = \frac{\int_0^{H_s} |u(x,y,t)|T(x,y,t)dy}{\int_0^{H_s} |u(x,y,t)|dy} \tag{6}$$

The heat transfer properties are also represented by the Colburn j factor, which is generally taken to be independent of the Prandtl numbers and a function of Re alone.

$$j = \frac{Nu}{RePr^{1/3}} \tag{7}$$

2.2 Numerical Method

The pre-processor GAMBIT 2.2.30 was used to generate grid points and cells. The solver FLUENT 6.2.16 was used to solve the fluid-dynamically and thermally algebraic equations cell by cell with various numerical schemes, and the post-processors C and TECPLOT 360 were used to evaluate and visualize the computed results. Referring to the algorithmic schemes of the solver, the finit-volume method and segregated scheme were used to solve these governing equations, with a second-order implicit scheme for transitional flow, a second-order scheme for solving pressure, and the third-order MUSCL (Monotone Upstream Scheme for Conservation Laws) scheme for solving the momentum and temperature. The PISO (Pressure-Implicit with Splitting of Operator) scheme was used for solving pressure-velocity coupling.

3. RESULTS AND DISCUSSION

Preserving a fixed space ratio, $L \equiv \hat{L}/\hat{H}_s$, and relative bump height, $H = \hat{H}/\hat{H}_s$, the corrugation angle of a bumped channel can be varied independently to encompass the limits of a wavy channel with β_{min} and a grooved channel with $\beta = 90\circ$. The results and discussion are organized in a similar progression, beginning with examination of the wavy channel limit, proceeding to consideration of variations in β for the bumped channel and finally, examination of the grooved channel limit.

3.1 Wavy Channel Limit

In a wavy or corrugated channel , only two independent parameters are necessary to fully specify the geometry. With a fixed aspect ratio, $L \equiv \hat{L}/\hat{H}_s$, and relative bump height, $H = \hat{H}/\hat{H}_s$, the corrugation angle is uniquely determined since

$$\beta = \tan^{-1}\left(\frac{4H}{L}\right). \tag{8}$$

With $H = 0.28$ and $L = 3.0$, the bump height and space ratio adopted in the present study, the corrugation angle is 20.5°. A further distinction of significance for the wavy channel is whether the main channel is blocked or open. For $2\hat{H} < \hat{H}_s$, a portion of the flow passage is unblocked, viewed in a streamwise direction. Clearly this is the case for the present geometry although this is often not so for many of the wavy channel investigations reported in the literature.

The primary oscillation frequency and transport properties for the wavy channel limit and a bumped channel with $\beta = 25°$ are shown in the first two rows of Table 2. The oscillation frequency increases for the slightly bumped channel as compared to the wavy channel. And while the time- and space-averaged Colburn j factor also increases,

the friction factor increases by a proportionally larger amount. The result is that while the j factor increases with β, the surface efficiency as reflected in $\bar{j}/\bar{f}$, decreases.

The time variation of the space-averaged j factor, j_s, and the space-averaged dimensionless wall shear stress, f_s, is shown in Figure 2. While the increase in f_s is readily apparent, other more subtle changes are also evident. The variation of j_s for $\beta = 25°$ is much less symmetric about its minimums and maximums than is the wavy channel limit. Apparently, the horizontal "bump" causes a change in the sequence of events composing an oscillation cycle.

Further insight is provided by local variations of j and f along the bottom wall of the domain, as shown in Figure 3, at the instants of their respective maximums in j_s. In both geometries, the minimum j occurs at the lower end of the separation wall and climbs rapidly along the recompression wall reaching a maximum prior to the exit lip of the bottom cavity. The maximum in the local j is clearly higher for the $\beta = 25°$ bumped channel than the wavy channel. In both geometries, the peak in the local wall shear stress is highest at the exit lip of the cavity. For the wavy channel geometry, this corresponds to the exit plane of the computational domain.

The strong qualitative similarities of the local j and f distributions are reinforced by consideration of the instantaneous streamlines shown in Figure 4, also at the instants of maximum j_s for the two geometries. Both geometries exhibit a separation vortex and a recompression vortex, the latter of which is repeatedly swept along the recompression wall and out of the cavity. Notice in both cases that the point of maximum j is downstream of the recompression vortex although elevated values are observed along much of the recompression wall due to this vortex.

3.2 Impact of Corrugation Angle

The effect of further increases in corrugation angle up to 65°, as shown in Table 2, are continued increases in the primary oscillation frequency and a near constant rate of

increase in the Colburn j factor for $\beta > 35°$. With the surface efficiency nearly constant for $\beta > 30°$, the higher heat transfer coefficients observed for higher β appear promising.

Additional insight into the impact of increasing corrugation angle is provided by consideration of the oscillation amplitudes for j_s and f_s. The data are shown in Figure 5 and in Table 3 for $30° \leq \beta \leq 65°$. The amplitude of the oscillations in f_s increase at a near constant rate whereas the oscillation amplitude for j_s appears to have asymptoted by $\beta \simeq 55°$. The amplitude of the oscillations in j_s appear to saturate while the time- and space-averaged values continue to climb. In contrast, there appears to be no such saturation in the f_s oscillation amplitude as its time- and space-averaged values climb with increasing β.

The increase in oscillation amplitude is also significant from the perspective of critical Reynolds numbers. Supercritical Hopf bifurcations exhibit an increase in oscillation amplitude which scales with $(\mathrm{Re} - \mathrm{Re}_c)^{1/2}$, where Re_c is the critical Reynolds number [8]. This suggests that the higher β geometries have a lower critical Reynolds number and would be expected to exhibit more favorable tradeoffs in transport behavior [9, 10].

Local variations of j and f are shown in Figure 6 for $\beta = 30°$ and $65°$ at their respective instants of maximum j_s. As observed for smaller values of β, the peak value of j is found at the exit bend of the cavity, with appreciable levels one either side of the corner. The maximum in f also coincides with this maximum in j. An additional peak in j is located at the entrance bend for the cavity, although j falls away rapidly after the corner separation. The minimum in j is located at the corner where the separation wall meets the cavity floor.

The instantaneous streamlines corresponding to Figure 6 are shown in Figure 7. The relatively weak vortices present along the separation wall limit the local j to relatively low values. Interestingly, at $\beta = 65°$, the bottom cavity has filled with three vortices. For $\beta = 35°$, the corresponding instant of maximum j_s reveals the presence of only two primary vortices.

3.3 Grooved Channel Limit

Increasing β to 90° produces a cavity with vertical walls, a geometry often termed a grooved channel. A channel with grooves on one side only was initially examined by Ghaddar et al. [11] in their investigation of stability and self-sustained oscillations. Their study revealed that the least stable wave modes corresponded to the Tollmien-Schlichting modes for the channel flow. In addition, the amplitude of the self-sustained oscillations indicated this transition was a regular Hopf bifurcation.

A channel with grooves on both channel walls, for $L = 3.0$ and $H = 0.28$, produces time- and space-averaged j and f values larger than for $\beta = 65°$. However, the increase in f is much larger than for j such that the goodness factor is significantly lower than the approximately constant value observed for $30° \leq \beta \leq 65°$. Interestingly, a one-sided grooved channel, with $H = 0.22$, is still subcritical at $\mathrm{Re} = 500$.

The time variation of j_s and f_s for these two cases are shown in Figure 8. For the singly-grooved channel, a steady asymptotic value of j_s is finally reached just over midway through the time integration period shown. The f_s is highly unsteady, with amplitudes much larger than that observed for j_s. The amplitude of the oscillations in f_s are slightly larger than for $\beta = 65°$, while the amplitude of the oscillations in j_s are nearly unchanged.

The distributions of local j and f for these two geometries are shown in Figure 9. Based upon observations for smaller β, maxima in j and f are expected near the entrance and exit corners of the bottom cavity. While this remains true for $\beta = 90°$, the increase in j and f is very steep on the cavity side of the exit lip, due to the 90° cavity wall. On the horizontal wall following this corner, both f and j decay much less rapidly. In a similar way, j and f increase as the separation corner is approached at the start of the bottom cavity. However, both fall off very quickly after the corner.

Instantaneous streamline and temperature contours for these two geometries are shown in Figure 10. The singly grooved channel reveals a core flow which is only

minimally disturbed by the presence of the groove, reflective of the fact that it remains subcritical at this Reynolds number. In contrast, the bumped channel with $\beta = 90°$ shows vigorous mixing of the main channel flow. Similar to the $\beta = 65°$ streamlines at its instant of maximum j_s, the $\beta = 90°$ streamlines show the bottom cavity filled by three distinct vortices.

3.4 Literature Comparisons

This paper examined a wide range of $\beta = 25 - 90°$ with a constant $Re = 500$. The prior studies focused on discussing the flow conditions with various Re under a small range of the β change, which differs from the objectives referred to in present results. The numerical results of $\bar{j}$ and $\bar{f}$ agree well with the experimental results of other fin geometries shown in Table 4. The values of both $\bar{j}$ and $\bar{f}$ increase when the β value increases, which indicates that heat transfer enhancement by corrugated angles modification has to take into account the increase in the friction factor. In additions, comparing the bumped fin of $\beta = 25°$ with flat and convex louvered fins of $\beta = 24.6°$ reveals that both the $\bar{j}$ and $\bar{f}$ values of louvered fins are larger than those of bumped fins, and which causes the $\bar{j}/\bar{f}$ value of bumped fins to be higher than the others because of the drastic flow destabilization of interrupted fins.

4. CONCLUSIONS

Seven selected corrugation angles ($\beta = 25 - 90°$) were compared to wavy ($\beta = 20.5°$) and grooved channels with the same space ratios, $L = 3$, relative bump height, $H = 0.28$, and Reynolds number. The bumped channels with large corrugation angles are shown to most strongly destabilize the channel flow, increasing $\bar{j}$, $\bar{f}$, and the oscillation frequency. The surface efficiency, $\bar{j}/\bar{f}$, is found to be essentially constant for $30° \leq \beta \leq 65°$. Backflows at the rear of the compression vortices produce the local minimums in the wall shear stress, f_{min}. The maximum local Colburn j and friction factors are observed upstream

of the compression vortex in each geometry. Comparing oscillatory amplitudes and frequencies, the heat transfer increases along with increased oscillatory frequencies, although the amplitudes of the oscillation saturate for $45° \leq \beta \leq 65°$. Increasing corrugation angle causes simultaneous increases in both the amplitudes and frequencies of the oscillations in the wall shear stress, f_s.

The wavy channel corresponds to the minimum corrugation angle for a given space ratio and relative bump height. The pattern of small corrugation angles exhibits the smallest values of $\bar{j}$, $\bar{f}$, and Ω. The surface efficiency is relatively large however, compared to the bumped channels. A singly grooved channel provides insufficient destabilization to the channel flow because this pattern possesses only one cavity and the flow regime is still subcritical with $Re = 500$. Its performance shows constant values of j_s, f_s, reflecting the subcritical steadiness.

References

[1] H. Zhang, X. Lang, The experimental investigation of oblique angles and interrupted plate lengths for louvered fins in compact heat exchangers, *Experimental Thermal and Fluid Science* 2 (1989): 100–106.

[2] K. Suga, H. Aoki, Numerical study on heat transfer and pressure drop on multilouvered fins, volume 4, ASME/JSME Thermal Engineering Proceedings. ASME. New York (1991) pp. 361–368.

[3] T. Hatada, T. Senshu, Experimental study on heat transfer characteristics of convex louver fins for air conditioning heat exchangers, Technical Report 84-HT-74, ASME paper (1984).

[4] N. C. DeJong, A. M. Jacobi, Localized flow and heat transfer in louvered-fin arrays, *International Journal of Heat and Mass Transfer* 46 (2003): 443–455.

[5] G. Comini, C. Nonino, S. Savino, Effect of space ratio and corrugation angle on convection enhancement in wavy channels, *Int J Num Methods Heat & Fluid Flow* 13 (2003): 500–519.

[6] N. C. DeJong, L. Zhang, A. M. Jacobi, S. Balachandar, D. Tafti, A complementary experimental and numerical study of the flow and heat transfer in offset strip-fin heat exchangers, *Journal of Heat Transfer* 120 (1998): 690–698.

[7] S. Patankar, C. Liu, E. Sparrow, Fully developed flow and heat transfer in ducts having streamwise-periodic variation of cross-sectional area, *Journal of Heat Transfer* 39 (1977): 80–86.

[8] E. P. L. Roberts, A numerical and experimental study of transition processed in an obstructed channel flow, *Journal of Fluid Mechanics* 260 (1993): 185–209.

[9] G. E. Karniadakis, B. B. Mikic, A. T. Patera, Minimum-dissipation transport enhancement by flow destabilization: Reynolds' analogy revisited, *Journal of Fluid Mechanics* 192 (1988): 365–391.

[10] H. Kozlu, B. B. Mikic, A. T. Patera, Minimum-dissipation heat removal by scale-matched flow destabilization, *Int. J. Heat Mass Transfer* 31 (1988): 2023–2032.

[11] N. K. Ghaddar, K. Z. Korczak, B. B. Mikic, A. T. Patera, Numerical investigation of incompressible flow in grooved channels. part 1. stability and self-sustained oscillations, *Journal of Fluid Mechanics* 163 (1986): 99–127.

[12] J. Y. Jang, L. K. Chen, Numerical analysis of heat transfer and fluid-flow in a three-dimensional wavy-fin and tube heat exchanger, *International Journal of Heat and Mass Transfer* 40 (1997): 3981–3990.

[13] M. Greiner, G. Speucer, P. F. Fischer, Direct numerical simulation of three-dimensional flow and augmented heat transfer in a grooved channel, *ASME J. Heat Transfer* 120 (1998): 717–723.

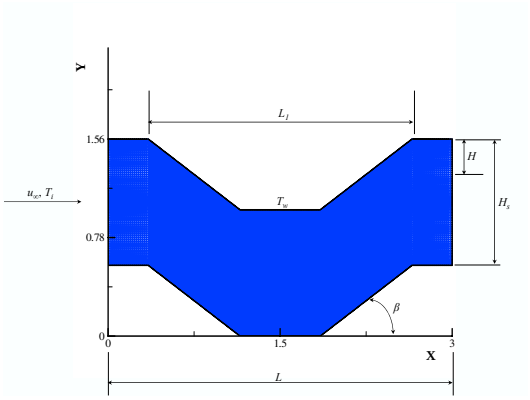

Figure 1 Schematic of problem geometry and representative grid distribution ($\beta = 35°$) for a periodic element in a bumped channel.

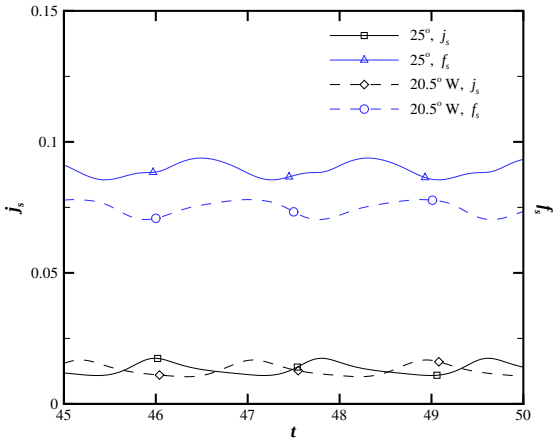

Figure 2 Comparison of space-averaged transport properties for the wavy channel and ($\beta = 20.5°$) the bumped channel ($\beta = 25°$).

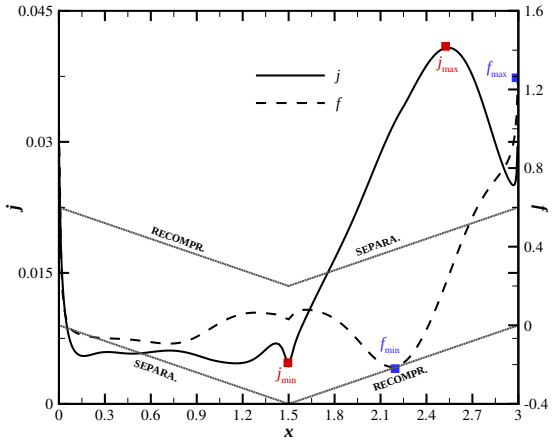

(a) $\beta = 20.5°$

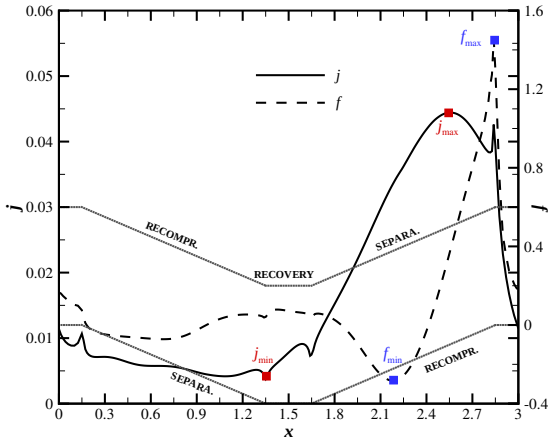

(b) $\beta = 25°$

Figure 3 Local j and f distributions at the instants of maximum j_s ($t = 47.06$ for $\beta = 20.5°$, $t = 45.99$ for $\beta = 25°$).

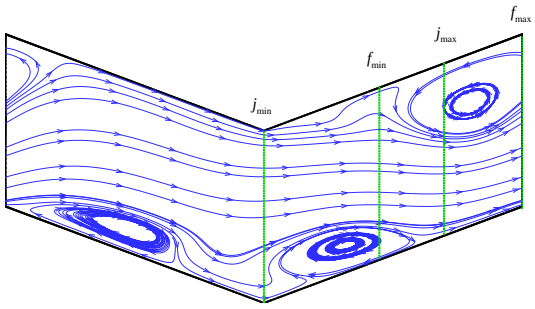

(a) $\beta = 20.5°$

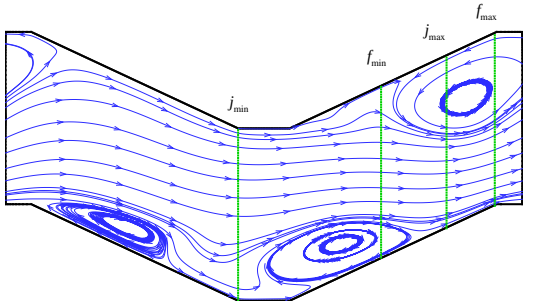

(b) $\beta = 25°$

Figure 4 Instantaneous streamline contours at the instants of maximum j_s ($t = 47.06$ for $\beta = 20.5°$, $t = 45.99$ for $\beta = 25°$). The positions of local minimums and maximums in j and f along the bottom wall are denoted by the vertical lines.

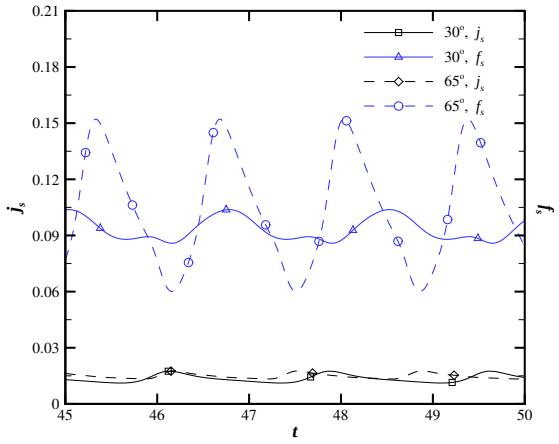

Figure 5 Time variation of transport quantities for $\beta = 30°$ and $65°$

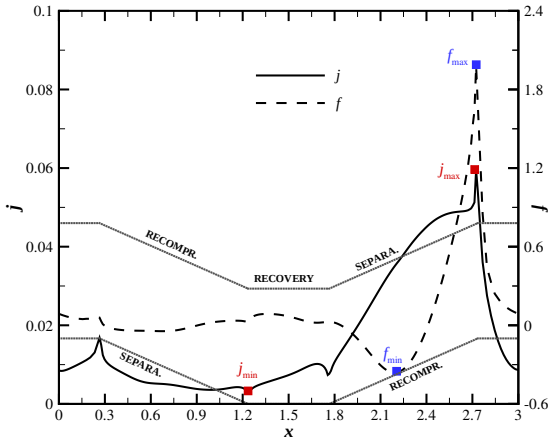

(a) $\beta = 30°$

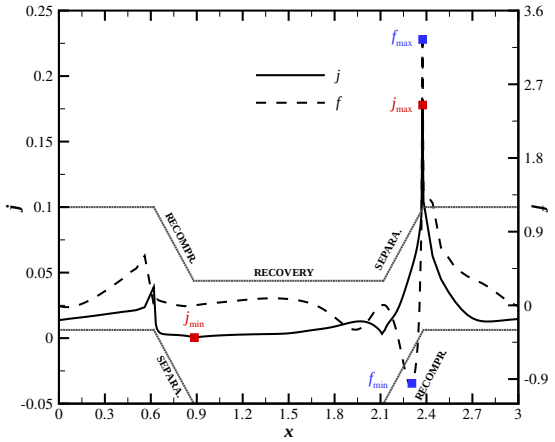

(b) $\beta = 65°$

Figure 6 Local j and f distributions at instants of maximum j_s ($t = 46.13$ for $\beta = 30°$, $t = 46.18$ for $\beta = 65°$).

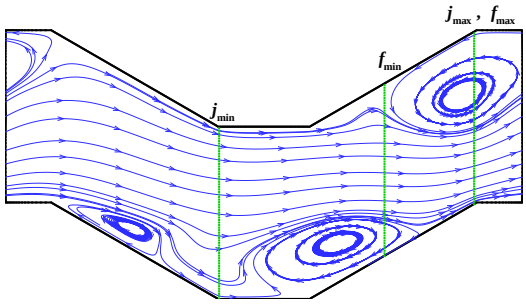

(a) $\beta = 30°$

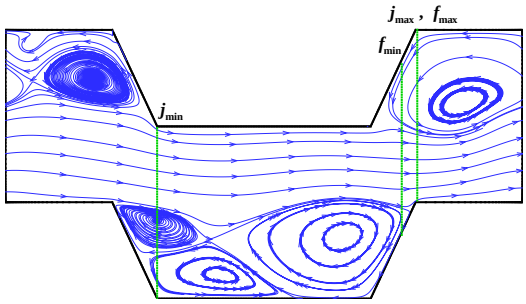

(b) $\beta = 65°$

Figure 7 Instantaneous streamline contours at instants of maximum j_s ($t = 46.13$ for $\beta = 30°$, $t = 46.18$ for $\beta = 65°$). The positions of local minimums and maximums in j and f along the bottom wall are denoted by the vertical lines.

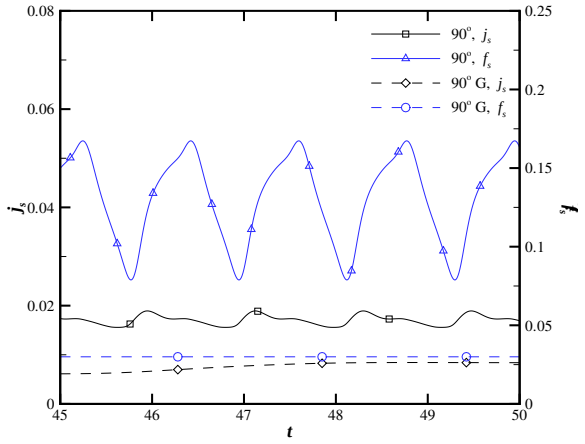

Figure 8 Comparison of space-averaged transport properties for the $\beta = 90°$ bumped channel and the singly-grooved channel.

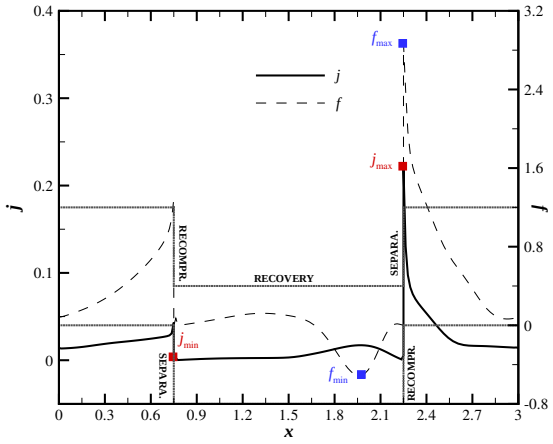

(a) $\beta = 90°$

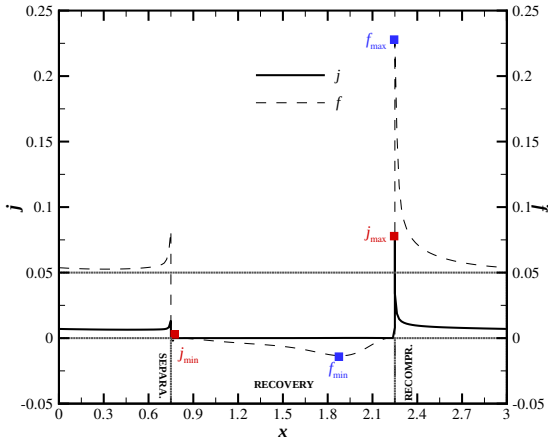

(b) $\beta = 90°$ (grooved)

Figure 9 Local j and f distributions at instants of maximum j_s for the bumped channel ($t = 45.95$ for $\beta = 90°$). The grooved channel is subcritical and the space-averaged j_s is time invariant.

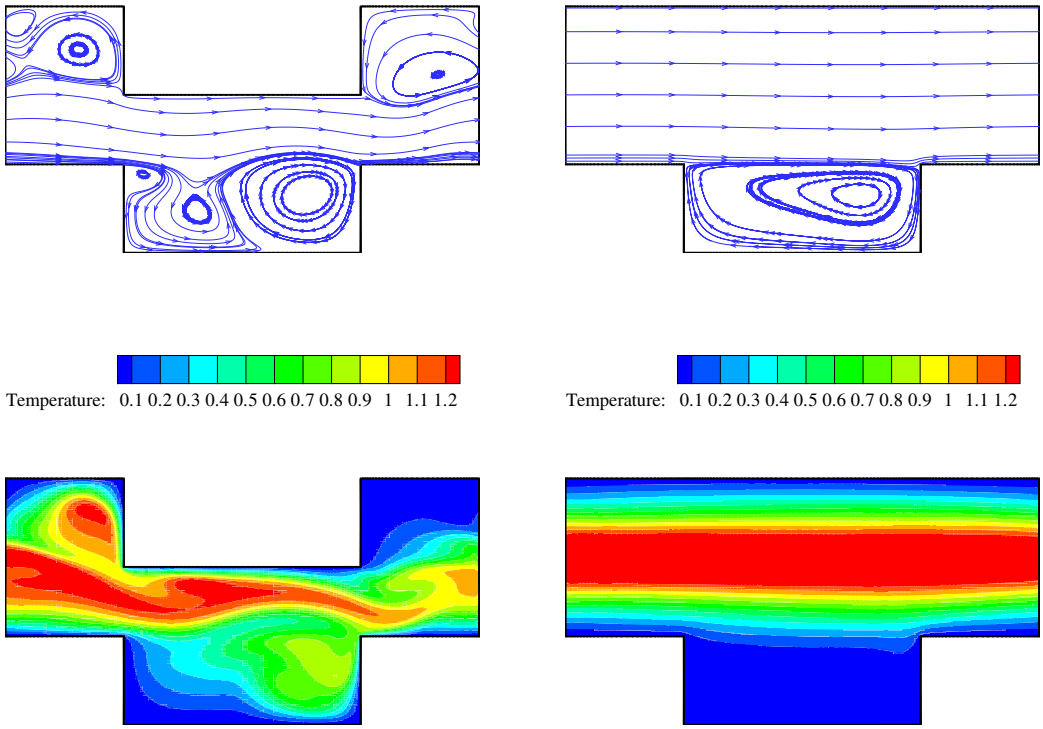

(a) $\beta = 90°$ (b) $\beta = 90°$ (Grooved)

Figure 10 Instantaneous streamline and temperature contours at the instant of maximum j_s for the bumped channel with $\beta = 90°$. The grooved channel is subcritical and the streamline and temperature contours are therfore steady.

Table 1 Geometric and numerical parameters of the cases investigated. For all cases, $L = 3$, $\triangle t = 0.002$ and $Re = 500$.

β	L_1	Cells	Nodes	CFL
20.5° W	3.00	20.480	20,817	0.49
25°	2.70	20,800	21,141	0.49
30°	2.47	21,280	21,627	0.49
35°	2.30	21,600	21,915	0.94
45°	2.06	22,400	22,761	0.52
55°	1.89	23,200	23,571	0.73
65°	1.76	24,000	24,381	0.88
90°	1.50	13,464	13,815	0.35
90° G	1.50	17,292	17,585	0.35

W-Wavy channel
G-Grooved channel

Table 2 Oscillation frequency and transport quantities. In all cases, $L = 3$, $Re = 500$.

Pattern	Ω	$\bar{j}$	$\bar{f}$	$\bar{j}/\bar{f}$
20.5° W	0.52	0.0130	0.075	0.173
25°	0.55	0.0134	0.089	0.151
30°	0.57	0.0135	0.093	0.145
35°	0.60	0.0137	0.094	0.146
45°	0.66	0.0141	0.099	0.142
55°	0.71	0.0146	0.102	0.143
65°	0.74	0.0150	0.104	0.144
90°	0.85	0.0171	0.129	0.132
90° G*	0.47	0.0084	0.030	0.280

* Subcritical

Table 3 Oscillatory characteristics of space-averaged transport quantities, j_s and f_s, for various β.

β	Max. j_s	Min. j_s	Max. j_s-Min. j_s	Max. f_s	Min. f_s	Max. f_s-Min. f_s
30°	0.0175	0.0112	0.0063	0.1038	0.0859	0.0179
35°	0.0172	0.0114	0.0058	0.1102	0.0794	0.0308
45°	0.0170	0.0124	0.0046	0.1232	0.0704	0.0528
55°	0.0173	0.0131	0.0042	0.1394	0.0664	0.0730
65°	0.0176	0.0133	0.0043	0.1521	0.0600	0.0921

Table 4 Comparison of $\bar{j}$, $\bar{f}$ and $\bar{j}/\bar{f}$ with different β values at $Re = 500$.

Type	β	$\bar{j}$	$\bar{f}$	$\bar{j}/\bar{f}$
Bumped fin	25°	0.0134	0.089	0.151
	30°	0.0135	0.093	0.145
	35°	0.0137	0.094	0.146
	45°	0.0141	0.099	0.142
	55°	0.0146	0.102	0.143
	65°	0.0150	0.104	0.144
	90°	0.0171	0.129	0.132
Flat louvered fin[3]	0°	0.0200	0.0660	0.303
	12.8°	0.0250	0.0910	0.275
	17.4°	0.0280	0.0960	0.292
	24.6°	0.0310	0.1040	0.298
Convex louvered fin [3]	9.7°	0.0288	0.0970	0.297
	17.4°	0.0331	0.1080	0.306
	20.7°	0.0350	0.1220	0.287
	24.6°	0.0388	0.1570	0.247
Wavy fin [5]	20°	0.0285	0.0484	0.589
Wavy fin and tube [12]	17.05°	0.0144	0.0567	0.254
Grooved channel [13]	45°	0.0048	0.0525	0.091

Impact of Three-Dimensional Characteristics on Convective Enhancement in Bumped Channel

Li-Kwen Chen and K. O. Homan
Department of Mechanical & Aerospace Engineering
Missouri University of Science & Technology
Rolla, Missouri 65409–0050, USA

Abstract

The previous study compared thermal and hydrodynamic performance of two-dimensional bumped channels with different space ratios and corrugation angles. A detailed three-dimensional numerical investigation of a bumped channel flow and heat transfer is presented ($L = \hat{L}/\hat{H}_s = 3$, $\beta = 35°$ and $Re = 200$ and 500) in this study. This channel has an aspect ratio of 3.7 to correspond with the reference fin height H_s. Continuous channels enhance heat transport due to the secondary instability generated by the corrugated surfaces. Secondary vortices, often termed longitudinal vortices. are revealed in the spanwise direction for the three-dimensional predictions. These vortices interact with the transverse vortices and lead to higher heat transfer and wall shear stress, as compared to the corresponding two-dimensional predictions. Comparison of local quantities at various cross sections illustrate the detailed influence of flow destabilization, developing viscous layers, and wall effects.

Nomenclature

Dimensional quantities are denoted by a hat, *e.g.* $\hat{t}$.

Roman

f local friction factor

H channel height

j	local Colburn j factor
j/f	goodness factor
L	channel length
s	wall coordinate
$\mathbf{n}$	unit normal vector
Nu	Nusselt number
p	pressure
Pe	Peclet number
Pr	Prandtl number
Re	Reynolds number
T	temperature
t	time
u, v, w	velocity components
W	Dimensional Width

Greek

α	thermal diffusivity
β	corrugation angle
Γ	time period
χ	perturbation amplitude parameter

μ	dynamic viscosity
ν	kinematic viscosity
ρ	density
σ	perturbation amplitude growth rate
τ	wall shear stress
Ω	frequency
Ψ	arbitrary scalar
ψ	Dimensionless Streamline

Subscripts and Superscripts

b	bulk
c	center
cr	critical
H	referenced to channel height
i	inflow
∞	free stream
min	maximum
min	minimum
w	wall
$-$	Time-and-Space-Averaged

1. INTRODUCTION

For certain applications in special fields, the surface geometry of an automotive radiator fin has to resist the particulate fouling problem. Conventional interrupted surfaces are excluded from utilization in these fields even though they considerably enhance heat transfer. Continuous surfaces augment heat transfer via secondary flow characteristics in a periodic corrugated channel. Various continuous channels provide complete intermixing due to flow separations and reattachments within the surfaces. Their geometries also influence the results of heat transfer and pressure drop under a given Reynolds number. The bumped fin is a newly product which is appropriate for dusty fields and performs a lower pressure drop than other continuous fins, such as wavy fins.

In the study of periodic bumped channels, numerical simulations are beneficial to investigate the detailed mechanisms with fully developed flow and theremal development.The channel flow behavior will gradually become three-dimensional as the Reynolds number increases. A two-dimensional model is gravely insufficient for depicting the longitudinal flow mechanisms [1].

Greiner *et al.* carried out a series of experimental and numerical studies in periodic grooved channels [2, 3, 4, 5]. These investigations disclosed that the Nusselt Numbers of two-dimensional simulations are 20% lower than those of three-dimensional results when the friction factors are lower by a factor of more than two at $Re = 1,000$ based on time-averaged velocity. Greiner *et al.* revealed that two-dimensional simulations underestimate flow performance generally, especially the friction drag, due to ignorance of longitudinal affects. Moreover, flow configurations will transit along with the Reynold numbers increase from a steady two-dimensional flow, to two- and three-dimensional wave structures, and then to three-dimensional mixing. In addition, the experimental passage is limited so that the flow was not synchronized in each groove and the long flat sections connected the end of the experimental apparatus. These two factors caused experimental flow unsteadiness

to be smaller than the numerical simulation. Two-dimensional simulations were incapable of accurately predicting $\bar{f}$ for $Re_a > 400$ or $\bar{j}$ for $Re_a > 1,000$. Three-dimensional simulations predicted $\bar{j}$ and $\bar{f}$ values within 20% of measured values as $800 < Re_a < 1,600$ [4].

One of Greiner *et al.*'s experimental studies employed a channel with an aspect ratio of 10:1, flat surfaces upstream and semi-grooved surfaces downstream for $Re = 300 - 15,000$ [3]. Two-dimensional traveling waves initially existed and then became three-dimensional wave configurations while the Reynolds number and distance from inlet increased.

Hwang *et al.* provided detailed illustrations to explain the relevant fluid mechanisms of continuous surfaces pertaining to a three-dimensional wavy duct with $Re = 1,000 - 5,000$, wavy angle=130 and 145°, and an aspect ratio of 7.3 [6]. Flow visualization results exhibit secondary vortices which are perpendicular to the streamwise direction. One is the counter-rotating secondary vortex, the Taylor-Görtler vortex, which is located in the middle region of a flow passage. The other is the corner kink generated on the wall corner. Flow separations and reattachments near the wall regions and then the main stream turns slightly away from the suction-side wall to the pressure-side wall because of the flow inertia force. In the wavy channel, these secondary vortices on the pressure-side wall, flow separations and reattachments on the suction-side wall, and corner vortices on the end walls periodically affect one another to augment the flow unsteadiness.

Periodic three-dimensional turbulent flow in a wavy duct was numerically and experimentally performed by Ergin *et al.* [7]. The various combinations of space ratios $(0.45 - 2)$ and corrugations angles ($\beta = 30$ and 45°) were carried out in the range of $Re = 2,000 - 10,000$. Comparison results exhibit that a decrease of the recirculation size with an increase in Re. As $\beta = 30°$, the size and strength of the recirculation increase with corrugation angles increase. In the region close to the side wall, the size and strength of the circulation decrease, more interactions between the main flow and the concave re-

circulation than the midregion. A seen in numerical comparisons of two-dimensional and three-dimensional models, both have better agreement in the main flow velocities than in the recirculation zone but two-dimensional models predict higher velocities than do three-dimensional ones. Along with increasing space ratios, both numerical predictions present agreeable friction factors with experimental results of $\beta = 30°$, but underestimate 31% the maximum value of the friction factor as $\beta = 45°$.

DeJong *et al*. combined complementary experimental and two-dimensional transient numerical analyses of the flow and heat transfer of various offset strip-fin geometries [8]. Numerical simulations afford detailed investigations of the fully-developed flow performance with an infinite periodic channel as a complement of a finite experimental array model. For Reynolds numbers above 1,300, the appearance of flow three-dimensionality would be remarkable. For Reynolds numbers below 1,000, thermal boundary conditions were important. Several fluid mechanisms were examined in this research, such as, boundary layer, flow separation, reattachment, wake formation and vortex shedding, which were all important for this complex geometry.

Fiebig investigated vortex generations of laminar channel flow via ribs, winglets, corrugations, and "hutzen" [9]. The results presented three enhancement mechanisms to increase convective heat transport: swirl, flow destabilization, and developing viscous layers. The vortex generator (VG) surfaces develop new viscous layer and transverse vortices (such as the Karman vortex) are typically generated in a periodic rib channel at $Re = 350$. Longitudinal vortices are characterized by the complex three-dimensional flow such as in a delta winglets channel. The flow in a two-dimensional corrugated channel generates counter-rotating longitudinal vortices (Taylor-Görtler vortices) because of the flow irregularities in concave regions. Both transverse vortices and longitudinal vortices can enhance with a low Re, but longitudinal vortices perform a more significant role than transverse vortices do for a given pressure drop.

Amon and Patera utilized a periodic grooved channel to explore the wall-bounded shear flow transition under different Reynolds number ranges by means of the spectral element method [10]. The heat transfer phenomenon was not discussed in their study, but showed the three-dimensional flow characteristic near criticality. The supercritical flow with a low Reynolds number was induced by grooved shear layer destabilization due to finite-amplitude Tollmien-Schlichting waves and three-dimensional secondary flow irregularities.

Robichaux et al. [11] investigated three-dimensional instabilities by using a two-dimensional square cylinder numerical simulation. The notable result included three kinds of three-dimensional disturbance modes: long-wavelength, short-wavelength, and intermediate-wavelength existing for Reynolds numbers at around 161, 190, and 200, respectively.

O'Brien and Sparrow [12] conducted an experimental study to obtain the forced convective heat transfer coefficients and the friction fictions for flows in a corrugated duct with $Re = 1,500 - 25,000$, $Pr = 4 - 8$ (water), a corrugation angle of 30°, and an aspect ratio of 10.

Previous two-dimensional simulations illustrated the thermal and hydrodynamic mechanisms within these channels. A two-dimensional model assumes that all performances in one direction are consistent. Therefore, some fluid mechanisms will not show in a two-dimensional configuration, especially for the supercritical regime. In reality, the fluid characteristics are synthetically influenced from three-dimensional orientations. This further study disclosed the impact of these mechanisms in three dimensions under the subcritical and supercritical regimes. Furthermore, the previous two-dimensional results will be compared to the present three-dimensional ones in this paper.

2. PROBLEM FORMULATION

2.1 Mathematical Model

When a numerical domain is assumed to be both hydrodynamically and thermally fully developed, suitably separated from channel the inflow and outflow effects, computational domain can be limited to a single module as shown in Figure 1. After a certain distance from the channel inlet, transfer mechanisms will repeat periodically from the inlet to the outlet. In the fully developed region, this repetition allows for analysis of a single module with one periodic length only [10]. In this numerical study, the whole fin array is simplified as a three-dimensional two-fin domain contained in a computational domain with a dimensionless length $L = 3$, a dimensionless height $H_s = 1$, and a dimensionless width $W = 3.7$, respectively.

The tensor forms of the dimensionless continuity, momentum, and energy equations can be written as

$$\frac{\partial u_i}{\partial x_i} = 0 \quad in\ D \tag{1}$$

$$\frac{\partial u_i}{\partial t} + \frac{\partial}{\partial x_j}(u_i u_j) = -\frac{\partial p}{\partial x_i} + \nu \frac{\partial^2 u_i}{\partial x_j \partial x_j} \quad in\ D \tag{2}$$

$$\frac{\partial T}{\partial t} + \frac{\partial}{\partial x_j}(T u_i) = \alpha \frac{\partial^2 T}{\partial x_j \partial x_j} \quad in\ D \tag{3}$$

Where the length scale is taken as $\hat{H}_s$, the velocity scale as $\hat{u}_\infty$, and the time scale as $\hat{H}_s/\hat{u}_\infty$. The definitions of the dimensions parameters are $Re_H \equiv \hat{u}_\infty \hat{H}_s/\nu$ and $Pe \equiv \hat{u}_\infty \hat{H}_s/\alpha$. Periodic boundary conditions can applied for velocity, pressure, and temperature according to the method originally proposed by Patankar et al. [13].

On the solid walls, the usual no-slip, $u = v = w = 0$, and a constant temperature boundary condition are used, $T = 0$. The inlet velocity is initially taken to be a uniform horizontal velocity, equal to that of the area-averaged dimensional velocity, $u = 1$, $v = 0$,

$w = 0$, and $T = 1$. The friction factor is defined in terms of the wall shear stress, τ_w, by

$$f = \frac{2\tau_w}{\rho u_\infty^2} \tag{4}$$

The heat transfer behavior is characterized by the Nusselt number, defined as

$$Nu = \frac{\frac{\partial T}{\partial n}|_w}{T_b} \tag{5}$$

where T_b is the dimensionless bulk mean temperature, which can be defined as

$$T_b = \frac{\int_0^{H_s} |u(x, y, z, t)| T(x, y, z, t) dy}{\int_0^{H_s} |u(x, y, z, t)| dy} \tag{6}$$

The heat transfer properties are also represented by the Colburn j factor, which is independent of the Reynolds and Prandtl numbers.

$$j = \frac{Nu}{RePr^{1/3}} \tag{7}$$

Space and time-averaged values of the j and f are defined as

$$\Psi_s(t) = \frac{s}{s} \int_0^l \Psi(x, y, t) dl \tag{8}$$

$$\bar{\Psi} = \frac{1}{\Gamma} \int_t^{t+\Gamma} \Psi_s(t) dt \tag{9}$$

where s is the coordinate along the wall and Γ is a period of at least two oscillation cycles in length.

2.2 Numerical Method

The pre-processor GAMBIT 2.2.30 was used to generate grid points and cells. The solver FLUENT 6.2.16 was used to solve the fluid-dynamically and thermally algebraic

equations cell by cell with various numerical schemes, and the post-processors C and TECPLOT 360 were used to evaluate and visualize the computed results. Referring to the algorithmic schemes of the solver, the finit-volume method and segregated scheme were used to solve these governing equations, with a second-order implicit scheme for time integration, a second-order scheme for solving pressure, and the third-order MUSCL (Monotone Upstream Scheme for Conservation Laws) scheme for solving the momentum and temperature. The PISO (Pressure-Implicit with Splitting of Operator) scheme was used for solving pressure-velocity coupling.

Mesh distributions and time step sizes ($\triangle t = 0.002$) of each computational module are based on the previous study. Cell numbers were modified by following the previous two-dimensional model to correspond with the CFL condition. Finer grid distributions are set near the boundary walls, the inlet and outlet, and the shear layer areas with $271 \times 21 \times 81$ (460,971 nodes) representing $X-$, $Y-$, and $Z-$directions, respectively.

3. RESULTS AND DISCUSSION

3.1 Transport Properties

In previous work, a two-dimensional slice of the present geometry ($L = 3$, $H = 0.28$) was examined and computed results included the critical Reynolds number, Colburn j factor, and friction factor. According to the literature, three-dimensional numerical predictions exhibit higher values of friction factors and Colburn j factors than do two-dimensional predictions [4, 8]. A comparison of the predicted j and f are shown in Table 1 at subcritical ($Re = 200$) and supercritical ($Re = 500$) Reynolds numbers. In the subcritical regime, the increases from the two-dimensional prediction to three-dimensional prediction in $\bar{j}$ and $\bar{f}$ values, are 41% and 15%, respectively. In the supercritical regime, the increases in $\bar{j}$ and $\bar{f}$ values are 36% and 29%, respectively. The difference between the two predictions is the impact of spanwise irregularities. In a two-dimensional model, all spanwise condi-

tions are presumed consistent. The two-dimensional model is therefore capably only of capturing transverse vortices as the fluid mechanisms to increase heat transport. While the two-dimensional results provide a basis for understanding the overall flow behavior, the flow physics not captured by the model limit its ability to predict the practical channel flow performance. In a three-dimensional simulation, however, longitudinal vortices can be observed and provide a mechanism to influence cross-sectional flow patterns in the spanwise direction. The effect of these flow structures is greater for the heat transfer than that for the wall shear stress. The increases in the predicted j and f are proportational at $Re = 500$, such that the goodness factor, $\bar{j}/\bar{f}$, is close for the 3-D prediction as for the 2-D prediction. As $Re = 200$, the change in the predicted goodness factor between the two- and three-dimensional models is larger.

Differences between the two-dimensional and three-dimensional predictions are also evident in the spaced-averaged values of j and f shown in Figure 2. The three-dimensional results exhibit a slightly higher oscillation frequency ($\Omega = 0.66$) than the two-dimensional results ($\Omega = 0.6$). Although the change in the primary oscillation frequency is moderate, the amplitude of the oscillations changes significantly, especially for the f_s. For both j_s and f_s, the amplitudes of the predicted oscillations are lower in the three-dimensional model. In the two-dimensional model, only the growth, translation and detachment of the transverse vortices cause the periodic behavior. In the three-dimensional model, this same sequence remains important but is tempered by the more complex spanwise variations.

An effect not immediately apparent in Figure 2 is the relatively long time to steady periodic behavior. As previously metioned, the steady periodic (or quasi-periodic) behavior is obtained from the long time integration of the Navier-Stokes equations from an arbitrary initial condition. Interestingly, the time necessary for the simulation to settle into a steady periodic behavior was noticeably less for the three-dimensional simulations as was the case for the two-dimensional simulations. The difference is evident in the time histroy of the j_s for a two-dimensional simulation. At $t \simeq 32.5$, the j_s variation predicted by the two-

dimensional prediction moves significantly closer to the three-dimensional prediction. As this "transition" occurs, the oscillation amplitude decreases and $j_s(t)$ draws much closer to that of the 3-D prediction.

Two other aspects of the results shown in Figure 2 are worth noting. The first is the relative smoothness of the j_s variation for the 3-D model as compared to the 2-D model. Presumably, the additional degrees of freedom available in the 3-D model allow for smoother transitions between the stages of the periodic oscillation.

3.2 Subcritical Behavior

In our earlier two-dimensional investigation, the critical Reynolds number for the bumped geometry with $L = 3$ was determined to be 300. The critical Reynolds number is a crucial indicator since when the flow regime is subcritical, secondary vortices show steady behaviors with constant sizes and shapes, doing little to improve heat transfer. In fact, these fixed vortices further compress the main flow region and generally serve to increase the thermal resistance. The anticipated steady behavior of j_s and f_s is indeed observed in the three-dimensional results, as shown in Figure 3 . The space-averaged transport quantities are indeed constant at the subcritical Reynolds number of 200 in the three-dimensional results, as they were in the two-dimensional results. The cause for the difference in the predicted steady value is clear upon examination of the streamline and temperature contours. The transverse vortices anticipated from the two-dimensional results are evident in only three of the selected cross sections for instantaneous streamlines, Y =1.85, 2.46, and 3.08, respectively, as shown in Figure 4.

3.3 Supercritical Behavior

As already observed, in the supercritical regime, the transport quantities exhibit a steady periodic behavior. The previous two-dimensional results have demonstrated that a single oscillation cycle corresponds to the growth, translation and finally ejection of a

transverse vortex from the bottom cavity. Although this basic cycle is present in the three-dimensional results, the detailed characteristics are altered by spanwise variations. To investigate this further, is focused on two instants in the oscillation cycle, instants at which the j_s reaches its maximum and minimum. The corresponding simulation time is indicated in Figure 2.

The instantaneous streamline and temperature contours at an instant of maximum j_s is shown in Figure 5. One aspect, immediately evident, is that transverse vortices extends across the entire spanwise width of the channel. This is in marked contrast to that observed in the subcritical regime. The intensity appears to diminish, however the $Y = 0$ sidewall. This transverse vortex in the bottom cavity is the transverse vortex in the concave half cavity along the top wall. This vortex is most intense on the pressure side of the channel. The vortices are also smaller in size than that at the subcritical *Re* of 200. The strong transverse vortex leads to high temperature gradients, particularly in the vicinity of $Y = 2.46$.

The instantaneous streamlines at an instant of minimum j_s ($t = 41.40$) are notably different, as shown in Figure 6. One obvious difference is that the bottom cavity is largely filled by a transverse vortex which spans essentially the entire channel width. This is precisely the flow field predicted by the two-dimensional simulations at the instant of minimum j_s as well.

The additional flow dynamics captured by the three-dimensional model are revealed by streamline contours in a streamline contours in a spanwise plane, as shown in Figure 7. The contours reveal the presence of longitudinal vortices, the cores of which move back and forth across the width of the channel. At the instant of maximum j_s, the axis of the longitudinal vortex is closest to the suction side wall, in the region where the transverse vortices are smallest.

The distributions of local j and f are shown in Figure 8 at an instant of maximum j_s. The locally highest values of j are observed immediately preceding the exit lip of the bottom cavity and just prior to the entrance lip of the bottom cavity. The heighest values

are also clustered toward the pressure side of the channel, where the transverse vortices have their greatest intensity. Near the sidewalls, the heat transfer rate is relatively low and exhibits only minimal variation in the flow direction.

As evident in Figure 8 (b), the locally highest values of f coincide with that of j values and therefore temperature gradients. The region near the exit lip of the bottom cavity is a source of locally high f across the width of the channel and does not diminish on approaching the $Y = 0$ sidewall near as rapidly as j does.

3.4 Literature Comparisons

The further three-dimensional study employed in this paper had a constant $Re = 500$. The difficulty of comparative evaluations is that the prior studies employed high Reynolds numbers to compare two-dimensional and three-dimensional predictions. The numerical results of $\bar{j}$ and $\bar{f}$ agree well with the experimental results of other fin geometries shown in Table 2. Values of both $\bar{j}$ and $\bar{f}$ increase when the β value increases, which illustrates that heat transfer enhancement by a modification of corrugated angles needs to take into account the increase in thermal resistance. In additions, the bumped fin of three-dimensional predictions perform larger results than the two-dimensional predictions because the three-dimensional simulation demonstrates the longitudinal swirls in the spanwise direction.

4. CONCLUSIONS

Numerical investigation of a three-dimensional bumped channel has been conducted at two Reynolds numbers, $Re = 200$ and 500. The predicted heat transfer and friction loss exhibit different levels of change between the subcritical and supercritical flow regimes, as compared to prior two-dimensional results. The $\bar{j}$ and $\bar{f}$ values increase 41% and 15% for the subcritical regime and increase 36% and 29% for the supercritical regime. The two-dimensional predictions of space-averaged j factor, j_s, do not draw close to the three-dimensional predictions until the time integration has proceeded for a relatively long time.

Comparing the predictions, the three-dimensional flow displays relatively smaller oscillatory amplitudes with a slightly higher oscillation frequency. Study results presented have shown that the three-dimensional prediction effects are more prominent in the subcritical regime than in the supercritical regime. The subcritical flow exhibits steady streamline and temperature contours while the supercritical behavior reveals a periodic behavior much like previous two-dimensional predictions. In the three-dimensional simulations, longitudinal vortices develop and disturb the spanwise flow distribution. Heat transfer enhancement by longitudinal vortices is more prominent in the supercritical flow regime. The longitudinal vortices move back and forth between the two sidewalls, alternately deflecting the main flow and increasing the local heat transfer rate. The heat transfer and wall shear stress are markedly higher near one of the two side walls. Since both the boundary conditions and grid are symmetric in the spanwise direction, this preference for one side wall may be due to a flow bifurcation although this possibility has not been investigated in detail. As with the two-dimensional predictions, the highest levels of heat transfer and wall shear stress are observed at the edges of the bumped cavity.

References

[1] M. Greiner, P. F. Fischer, H. M. Tufo, R. A. Wirtz, Three-dimensional simulations of enhanced heat transfer in a flat passage downstream from a grooved channel, *ASME J. Heat Transfer* 124 (2002): 169–176.

[2] M. Greiner, P. F. Fischer, H. Tofu, Two-dimensional simulations of enhanced heat transfer in an intermittely grooved channel, *ASME J. Heat Transfer* 124 (2002): 538–545.

[3] M. Greiner, R. F. Chen, R. A. Wirtz, Heat transfer augmentation through wall-shape-induced flow destabilization, *ASME J. Heat Transfer* 112 (1990): 336–341.

[4] M. Greiner, R. J. Faulkner, V. T. Van, H. M. Tufo, P. F. Fischer, Simulations of three-dimensional flow and augmented heat transfer in a symmetrically grooved channel, *ASME J. Heat Transfer* 122 (2000): 653–660.

[5] M. Greiner, G. Speucer, P. F. Fischer, Direct numerical simulation of three-dimensional flow and augmented heat transfer in a grooved channel, *ASME J. Heat Transfer* 120 (1998): 717–723.

[6] S. D. Hwang, H. H. Kim, H. H. Cho, Heat transfer in wavy duct with different corrugation angle, in: ASME International Mechanical Engineering Congress (2002).

[7] S. Ergin, M. Ota, H. Yamaguchi, Numerical sudy of periodic turbulent fow trough a corrugated duct, *Numerical Heat Transfer, Part A* 40 (2001): 139–156.

[8] N. C. DeJong, L. Zhang, A. M. Jacobi, S. Balachandar, D. Tafti, A complementary experimental and numerical study of the flow and heat transfer in offset strip-fin heat exchangers, *Journal of Heat Transfer* 120 (1998): 690–698.

[9] M. Fiebig, Vortices: Tools to influence heat transfer-receent developments, in: Proceedings of the 2nd European Thermal-Sciences and 14th UIT National Heat Transfer Conference, volume 1 (1996) pp. 41–56.

[10] C. H. Amon, A. T. Patera, Numerical calculation of stable three-dimensional tertiary states in grooved-channel flow, *Physics of Fluids A* 1 (1989): 2005–2011.

[11] J. H. Robichaux, S. Balachandar, S. P. Vanka, Three-dimensional instability of the wake of square cylinder, *Physics of Fluids* 11 (1999): 560.

[12] J. E. O'Brien, E. M. Sparrow, Corrugated-duct heat transfer, pressure drop and flow visualization, *ASME J. Heat Transfer* 104 (1982): 410–416.

[13] S. Patankar, C. Liu, E. Sparrow, Fully developed flow and heat transfer in ducts having streamwise-periodic variation of cross-sectional area, *Journal of Heat Transfer* 39 (1977): 80–86.

[14] T. Hatada, T. Senshu, Experimental study on heat transfer characteristics of convex louver fins for air conditioning heat exchangers, Technical Report 84-HT-74, ASME paper (1984).

[15] J. Y. Jang, L. K. Chen, Numerical analysis of heat transfer and fluid-flow in a three-dimensional wavy-fin and tube heat exchanger, *International Journal of Heat and Mass Transfer* 40 (1997): 3981–3990.

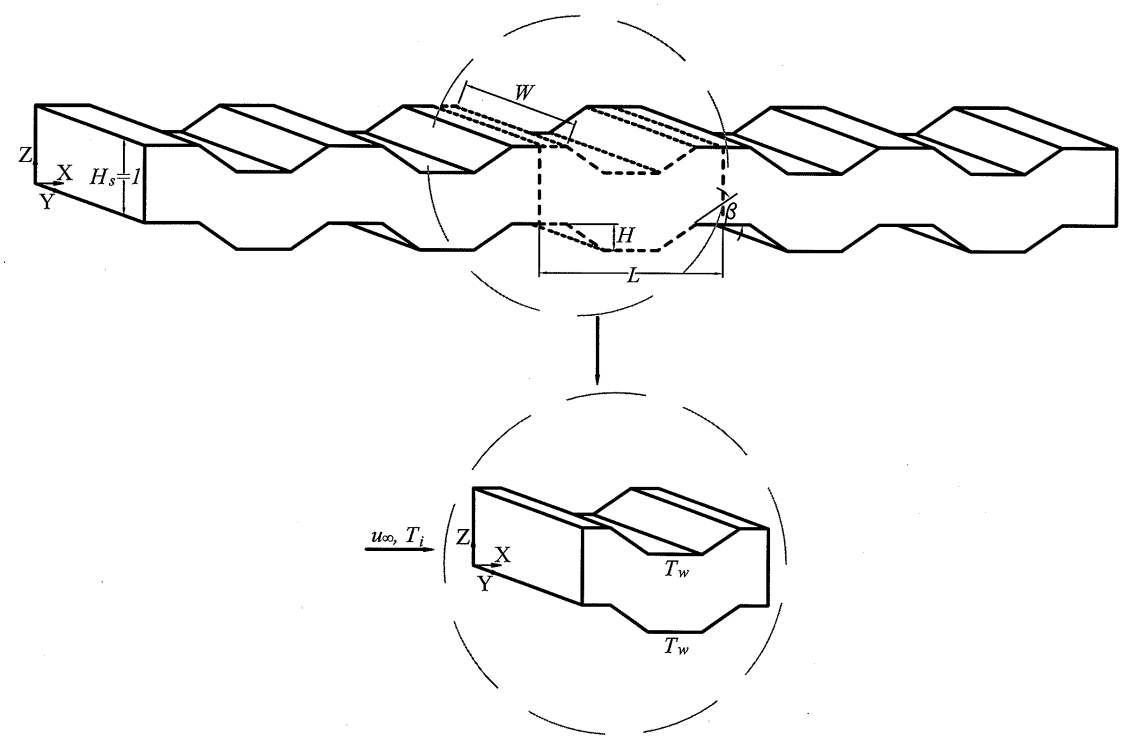

Figure 1 Schematic of the bumped channel arrangement. ($L = 3$, $W = 3.7$, $H = 0.28$, $\beta = 35°$) (The dashed line indicateds the computational domain in the fuly developed region.)

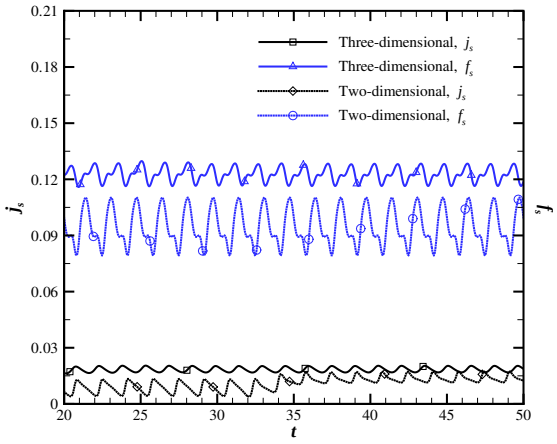

Figure 2 j_s and f_s comparisons of three-dimensional and two-dimensional models, $Re = 500$.

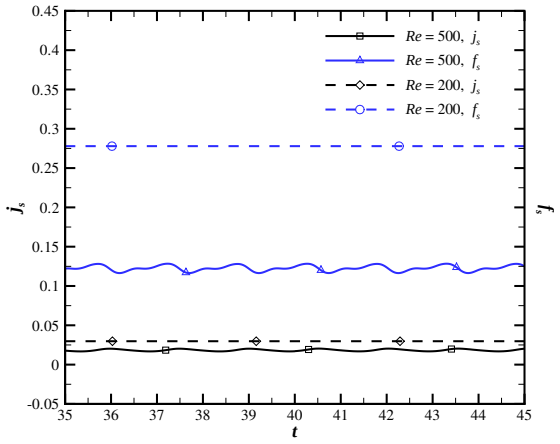

Figure 3 j_s and f_s comparisons of supercritical ($Re = 500$) and subcritical ($Re = 200$) regimes.

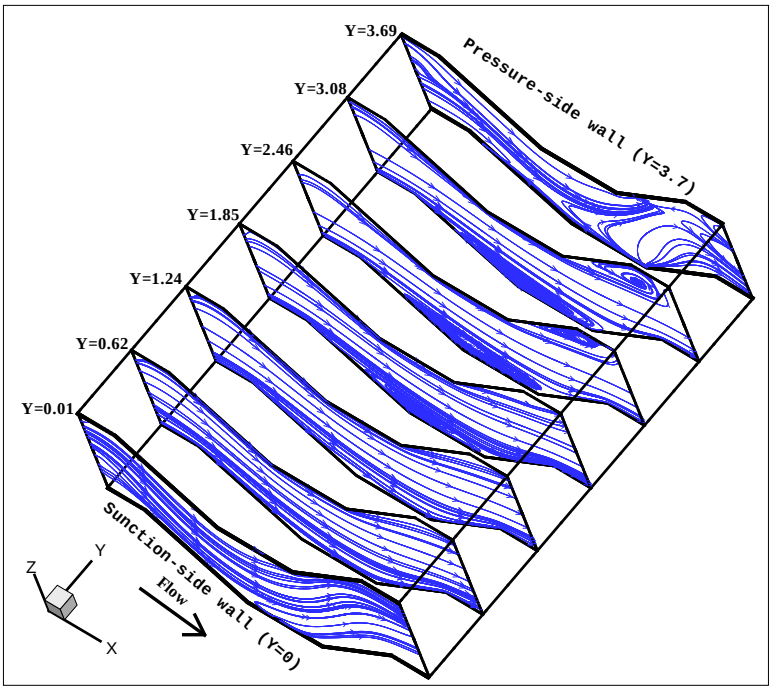

(a) $\psi(x)$

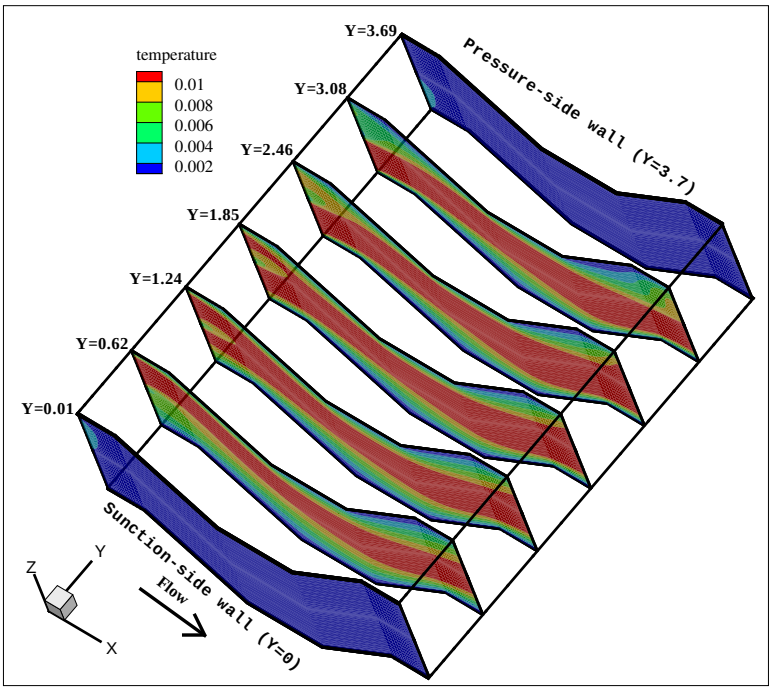

(b) $T(x)$

Figure 4 Steady streamline and temperature contours in the subcritical regime, $Re = 200$.

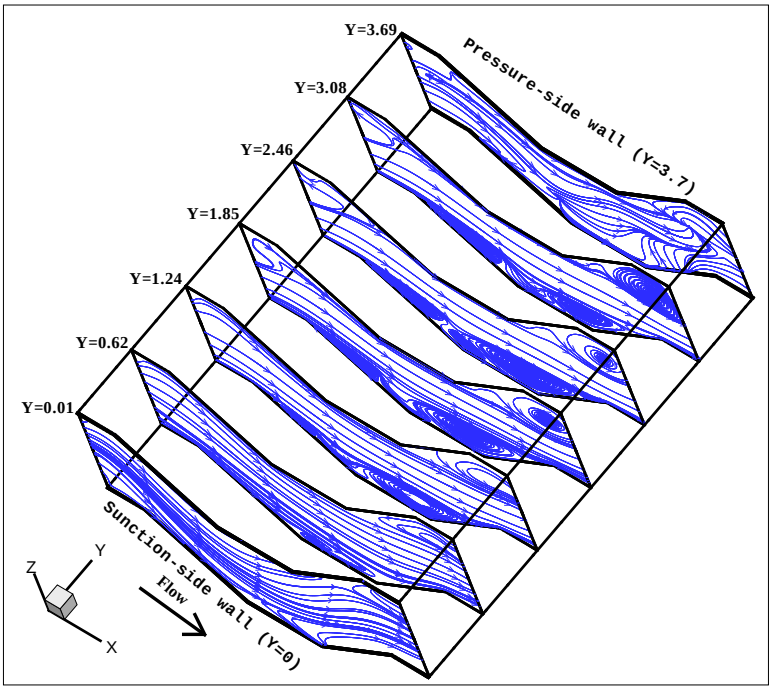

(a) $\psi(x,t)$

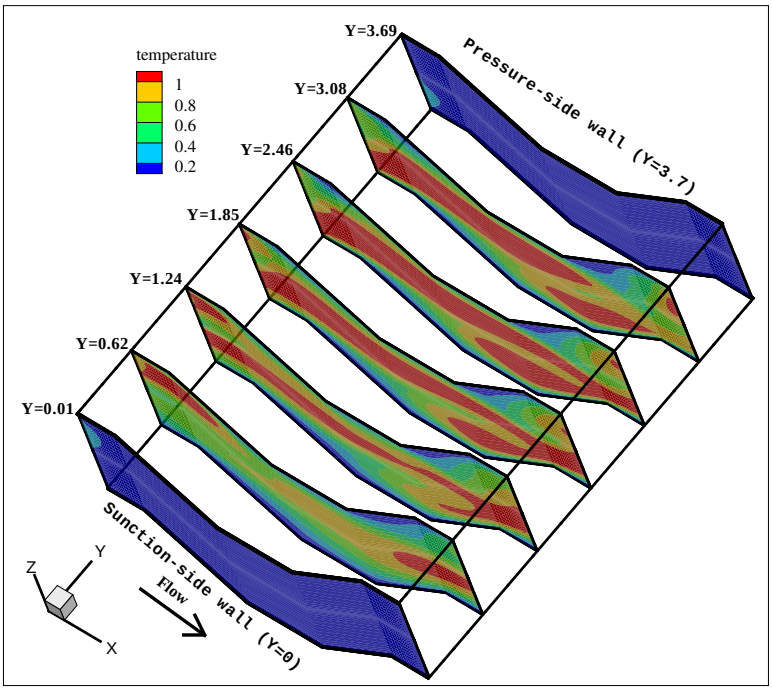

(b) $T(x,t)$

Figure 5 Instantaneous streamline and temperature contours for the steady periodic behavior at the instant of maximum j_s ($t = 40.52$) for $Re = 500$ in the supercritical regime.

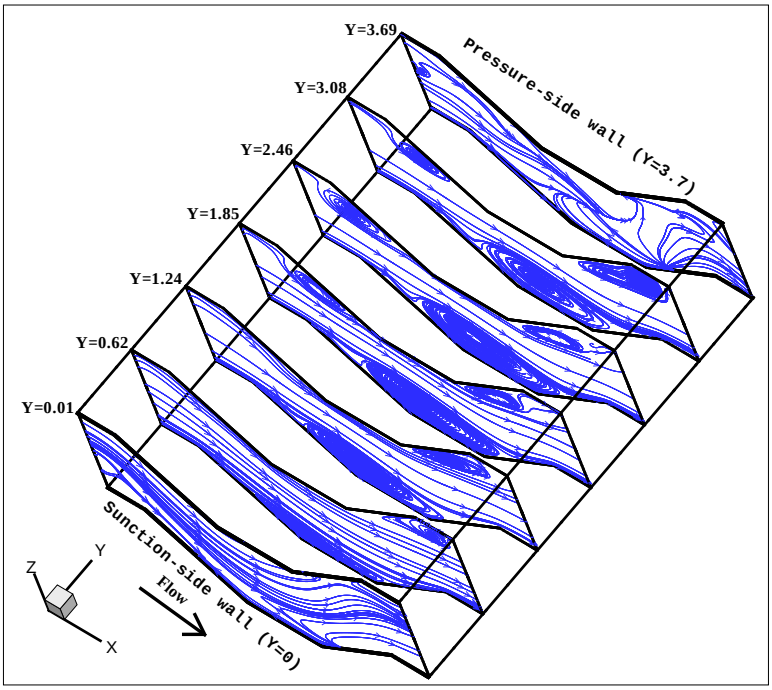

(a) $\psi(x,t)$

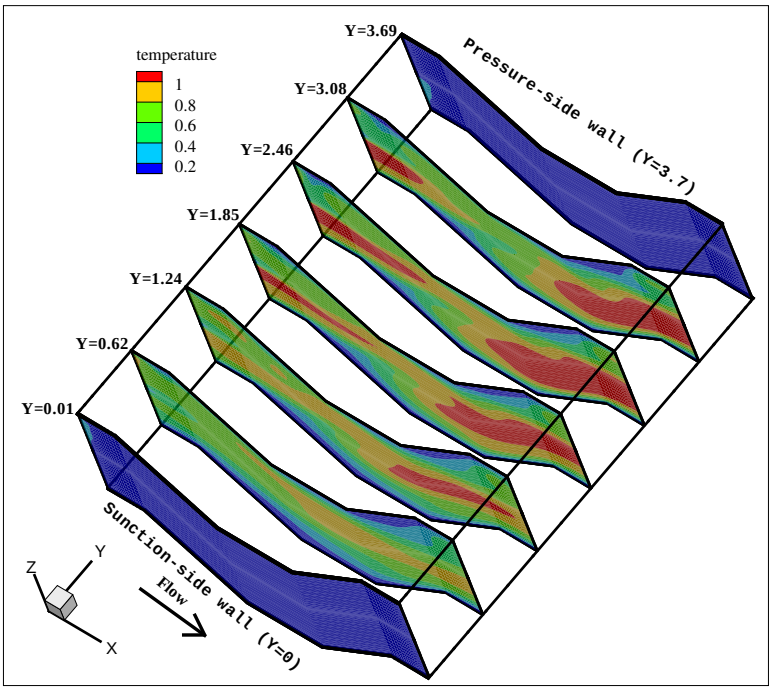

(b) $T(x,t)$

Figure 6 Instantaneous streamline and temperature contours for the steady periodic behavior at the instant of minimum j_s ($t = 41.40$) for $Re = 500$ in the supercritical regime.

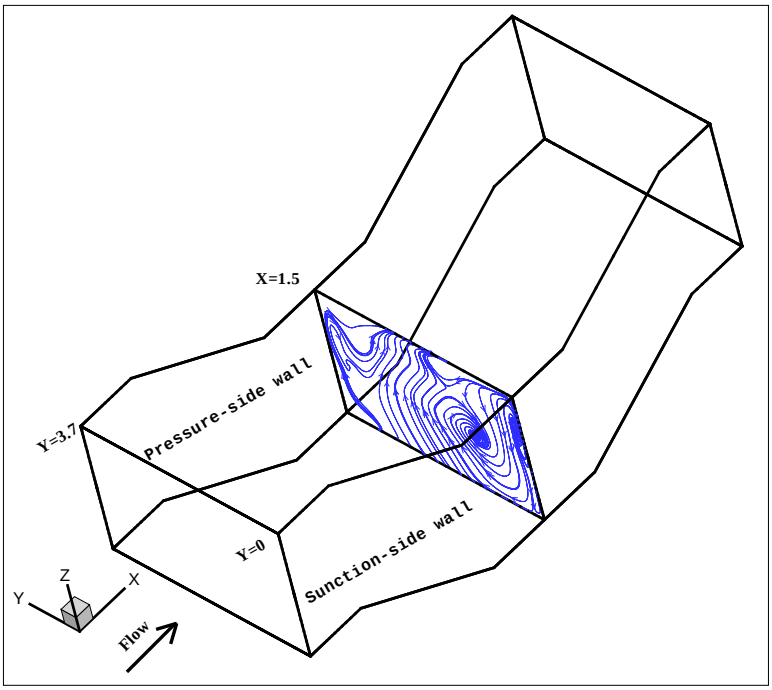

(a) Corresponding streamline contours ($t = 40.52$ of Maximum j_s)

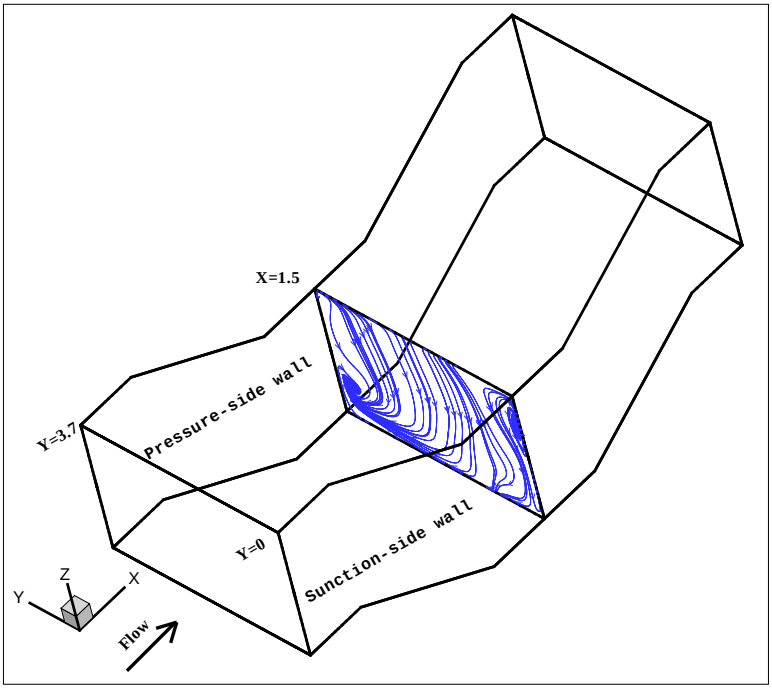

(b) Corresponding ctreamline contours ($t = 41.40$ of Minimum j_s)

Figure 7 Spanwise flow characteristics at the concave region, $Re = 500$.

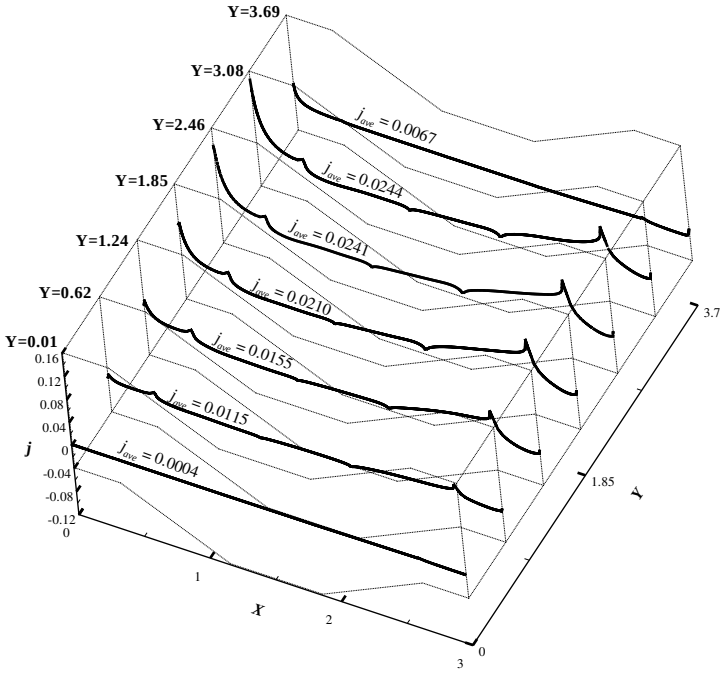

(a)

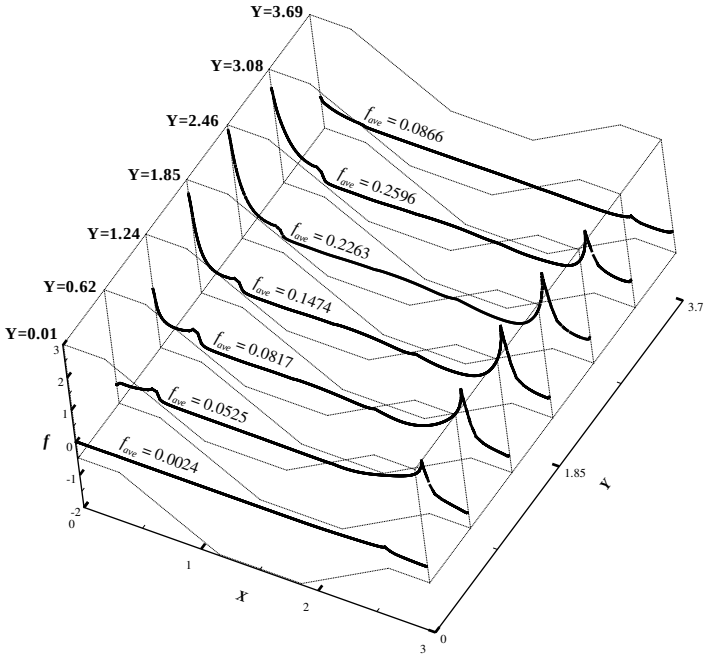

(b)

Figure 8 Instantaneous distributions of (a) j and (b) f in the transverse direction at an instant of maximum j_s ($t = 40.52$) for $Re = 500$ in the supercritical regime.

Table 1 Time-and-space-averaged scalars comparisons of three-dimensional and two-dimensional simulations at select Reynolds numbers.

Re	Simulation	$\bar{j}$	$\bar{f}$	$\bar{j}/\bar{f}$
200*	3-D	0.0297	0.278	0.107
	2-D	0.0211	0.241	0.088
500**	3-D	0.0187	0.123	0.152
	2-D	0.0137	0.094	0.146

* Subcritical
** Supercritical

Table 2 Comparison of $\bar{j}$, $\bar{f}$ and $\bar{j}/\bar{f}$ with different β values at $Re = 500$.

Type	β	$\bar{j}$	$\bar{f}$	$\bar{j}/\bar{f}$
Bumped fin (Three-dimensional)	35°	0.0187	0.123	0.152
Bumped fin (Two-dimensional)	35°	0.0137	0.094	0.146
Wavy fin [1]	20°	0.0285	0.0484	0.589
Grooved channel [5]	45°	0.0048	0.0525	0.091
Flat louvered fin [14]	0°	0.0200	0.0660	0.303
	12.8°	0.0250	0.0910	0.275
	17.4°	0.0280	0.0960	0.292
	24.6°	0.0310	0.1040	0.298
Convex louvered fin [14]	9.7°	0.0288	0.0970	0.297
	17.4°	0.0331	0.1080	0.306
	20.7°	0.0350	0.1220	0.287
	24.6°	0.0388	0.1570	0.247
Wavy fin and tube [15]	17.05°	0.0144	0.0567	0.254

VITA

Li-Kwen Chen was born on January 26, 1970 in Taipei, Taiwan. In June 1991, he graduated with a B.S. degree in Mechanical Engineering from National Chiao-Tung University, Hsinchu, Taiwan. After his military service as an artillery lieutenant from July 1991 to May 1993, he passed the entrance exam for National Cheng-Kung University, Tainan, Taiwan in August 1994. He subsequently began graduate studies there under Dr. Jin-Yuh Jang. He obtained his M.S. degree in Mechanical Engineering in June 1996. For the following seven years, he worked as a Professional Mechanical Engineer. During the fall of 2003 he enrolled at the University of Missouri-Rolla (UMR) in the Department of Mechanical & Aerospace Engineering. He began his graduate work under Dr. Kelly Homan in January 2005. In May 2008, he graduated from Missouri S&T with his Ph.D. degree in Mechanical Engineering.